ELSEVIER

Full Length Article

New insights into thermal processes of metal deposits on h-BN/Rh(1 1 1): A comparison of Au and Rh

Gábor Vári [a], Csaba Vass [b], Gyula Halasi [b,c], László Szabó [c], Krisztián Palotás [a,d], Péter Dombi [b,d], András Berkó [a], László Óvári [a,b,*], Zoltán Kónya [a,c]

[a] ELKH-SZTE Reaction Kinetics and Surface Chemistry Research Group, Rerrich Béla tér 1., H-6720 Szeged, Hungary
[b] Extreme Light Infrastructure – ELI ALPS, ELI-HU Non-Profit Ltd., Wolfgang Sandner u. 3., H-6728 Szeged, Hungary
[c] Applied and Environmental Chemistry Department, University of Szeged, Rerrich Béla tér 1., H-6720 Szeged, Hungary
[d] Wigner Research Center for Physics, Konkoly-Thege Miklós út 29-33., H-1121 Budapest, Hungary

ABSTRACT

In this paper the thermal properties of Au and Rh deposits are compared on hexagonal boron nitride (h-BN) "nanomesh" prepared on Rh(1 1 1), applying STM, XPS, low energy ion scattering (LEIS), LEED, and DFT. At room temperature, both metals essentially follow Volmer-Weber (3D) growth. Upon subsequent annealing, agglomeration (sintering), intercalation, and desorption are competing surface processes for both metals. For the more reactive Rh, we suggest an additional encapsulation mechanism: between 600 K and 750 K, fragments of decomposed h-BN diffuse locally from the bottom onto the metal clusters covering them partially. STM data indicates that agglomeration of gold nanoparticles proceeds faster compared to rhodium. At higher temperatures (~1050 K–1100 K), all non-desorbing gold atoms diffuse below h-BN, even for large initial coverages. On the other hand, for larger Rh deposits ($\geq$5 ML), the outermost layer always contains Rh. Accumulation of gold at the interface between h-BN and Rh(1 1 1) significantly enhances the thermal stability of h-BN, attributed to the lower reactivity of Au in the decomposition of h-BN compared to Rh(1 1 1). At elevated substrate temperatures, intercalation of individual adatoms takes place during deposition, which requires higher temperatures for rhodium due to its slower diffusion and higher probability of nucleation.

1. Introduction

Hexagonal boron nitride (h-BN) is an intensely studied two dimensional (2D) material [1–3]. Structurally it is a graphene analogue with a honeycomb lattice. However, the hexagons consist of alternating B and N atoms, and the difference in electronegativity between these elements leads to an insulator electronic structure. Because of its chemical inertness, chemical and thermal stability, h-BN is a useful insulating component of nanoelectronics, and is applied in lateral and vertical heterostructures [4–6].

h-BN monolayers have been typically synthetized on close packed metal surfaces [7,8,17,18,9–16], but not exclusively [19–22]. In a few cases, h-BN was prepared on alloys, like on PtRh(1 1 1) [23] and on Au/Rh(1 1 1) [24]. The lattice mismatch and the strength of chemical interaction between boron nitride and the metal are key factors governing structure and morphology of the h-BN overlayer. The interaction with coinage metals (Cu, Ag, Au) is weak, which results in a (nearly) flat

h-BN monolayer and a relatively large metal – nitride distance [11,16,25–27]. Since Au(1 1 1) is too inert to decompose borazine ($B_3N_3H_6$), the most frequently applied h-BN precursor, alternative approaches have been implemented, such as deposition by magnetron sputtering [28]. As an alternative route to prepare h-BN supported by gold, first the nitride was synthetized on Ni(1 1 1), followed by the deposition and intercalation of Au [29,30].

Ruthenium and rhodium bind boron nitride strongly. The energetically preferred bonding of h-BN to Rh(1 1 1) and Ru(0001) is with N atoms at on top position [26]. In the regions, where this is closely fulfilled ("pores"), the nitride – metal distance is relatively small. However, this arrangement cannot be realized everywhere, because of the considerable lattice mismatch between h-BN and the metal substrate (−7.7 % for Rh(1 1 1), and −8.2 % for Ru(0001)). In these areas ("wires"), the h-BN layer is located farther from the metal surface, resulting in a periodic undulation of the h-BN monolayer ("nanomesh") [13,17,18,26,31,32]. Although the nanomesh formation is most known

* Corresponding author.
 E-mail addresses: ovari@chem.u-szeged.hu, laszlo.ovari@eli-alps.hu (L. Óvári).

for Rh(1 1 1) and Ru(0001), it has been observed on Ir(1 1 1) and Re (0001), too [33–36]. A more appropriate approach is to consider stronger or weaker corrugation, and varying size of pore regions than the existence or non-existence of the nanomesh morphology of h-BN on transition metals, at least where some lattice mismatch exists [14]. When h-BN was prepared on Au/Rh(1 1 1) surface alloys, it was proven that the lateral pore size can be fine tuned by varying the gold content [24].

The growth of metals, deposited on h-BN via physical vapor deposition (PVD), have also been intensely studied applying different metal supports [2,17,44–48,24,37–43]. The nanomesh can serve as an eggbox-like template, since pores have frequently been observed to be preferential adsorption sites for organic molecules and metals [2,49], including gold [24,39,40,43,45,48], platinum [46,47] and iridium [48]. Conversely, Ni and Ag atoms are not trapped by the pores at room temperature, leading to the formation of large nanoparticles [45,50]. Similarly, according to density functional theory (DFT) calculations, Pd and Ni adsorption are not region specific on the h-BN/Rh(1 1 1) nanomesh [45]. However, after the deposition of size selected Pd_{19} clusters on h-BN/Rh(1 1 1), the nanoparticles were located inside the pores and were mostly adsorbed at their rim [51]. The PVD growth of metals on h-BN at room temperature mostly results in 3D nanoparticles [17,37,42], like Au on h-BN/Rh(1 1 1), when the clusters are not too small (they consist of more than cca. 30 atoms) [24,38,43], because the metal – nitride interaction is relatively weak compared to metal–metal interaction. The clusters prepared on the nanomesh are often characterized by a narrow size distribution, which makes these systems well-suited model catalysts [52–54]. Interestingly, the formation of two dimensional gold nanoparticles has been reported on h-BN/Ru(0001) [39] and on graphene/Ru(0001) [55], with the moiré patterns detectable on the Au platelets, too. An effect of the substrate temperature on the sticking coefficient was found for Co deposition on h-BN/Ni(1 1 1) [37].

Following metal deposition and early nucleation, agglomeration (sintering, coalescence), intercalation and desorption are all possible thermally activated processes, although, it is usually difficult to address the branching of the different channels quantitatively. In this paper, intercalation is termed as the diffusion of admetal below the h-BN monolayer, independent of whether the admetal is stabilized between the nitride and the topmost substrate atomic plane, or the admetal is incorporated/alloyed in the surface or bulk of the substrate. Regarding the mechanism of agglomeration, both Ostwald [46,51] and Smoluchowski [47,48] ripening have been postulated. On h-BN/Ir(1 1 1), the Ir nanoparticle array proved to be remarkably stable up to 700 K [48]. Intercalation took place during Co deposition at 450 K on h-BN/Ni(1 1 1) [37]. Similarly intercalation was reported upon annealing a h-BN/Rh (1 1 1) nanomesh covered by Mn nanoparticles at ~650 K [42], and also for Ir and Pt nanoclusters on h-BN/Ir(1 1 1) at T ≥ 750–850 K [47,48]. In each case, the process was accompanied by a 3D → 2D transition, as it was typically proven by STM and occasionally also by photoemission. In other cases, e.g. for Pt/h-BN/Rh(1 1 1), no intercalation was found up to 800 K [46]. Regarding the mechanism of intercalation, for Co/h-BN/Ni (1 1 1) it was emphasized that the intercalated 2D islands were located at defect lines of h-BN, which act as "collectors'' for Co, which intercalates. On nanomeshes, for Mn/h-BN/Rh(1 1 1) and Ir/h-BN/Ir(1 1 1) it was found that intercalation is quite local and does not (exclusively) proceed at distant defect sites, but a more detailed mechanism has not been proposed [42,48]. Upon annealing Mn/h-BN/Rh(1 1 1) at 773 K, the reverse process (escape of admetal atoms from below h-BN) and desorption also took place [42]. Heating 1 ML of Au up to 1050 K on h-BN/Ru(0001) led to intercalation and surface alloying, but the nanomesh morphology was still perceptible [39].

In our recent paper, the intercalation of Au below h-BN on Rh(1 1 1) was proven upon heating up to 1050 K by the comparison of low energy ion scattering (LEIS) and X-ray photoelectron spectroscopy (XPS) results. Formation of 2D islands were not reported over this process followed by STM, from which it was concluded that a 3D-2D transition is

not a prerequisite for intercalation [24]. Nevertheless, intercalated admetal certainly forms 2D features at appropriate coverage and temperature conditions. Naturally, in some cases it can be alloyed with the substrate metal or diffuse and join to substrate steps below the h-BN cover layer without the appearance of extended 2D nanocrystallites.

The above literature survey underlines that the mechanism of intercalation and other thermally activated processes is still quite elusive. In this work we present a comparative study on the thermal behavior of Au and Rh deposited on h-BN/Rh(1 1 1). It was expected that substantial details can be obtained about the complex mechanism of diffusion, desorption, intercalation and alloying processes by following the change of surface and subsurface chemical composition and morphology as well. Note, that from the point of view of alloying, Rh and Au are bulk immiscible, while deposited Rh is of course a completely mixing partner of the Rh(1 1 1) support by its nature. According to the bulk Au-Rh phase diagram, the solubility of Au in Rh is very small, less than 0.3 % up to 1340 K, while the solubility of Rh in Au is 1.5 % at the same temperature [57]. Nevertheless, gold on Rh(1 1 1) forms both ordered and random surface alloys in the outermost atomic layer [56]. Another interesting aspect of this study is that we extended our investigation up to a higher number of deposited layers (10 ML), accordingly the system imitates a h-BN nanosheet closed inside a bulk metal, consequently, it can provide a model system for metal-cluster/2D-material nanocomposites. Moreover, we address specifically the thermal stability of the h-BN monolayer, and the effect of admetals on it.

2. Material and methods

The experiments were performed in different ultrahigh vacuum (UHV) systems. Room temperature STM measurements were carried out in the first one, while the second one hosted an XPS and LEIS apparatus. Low energy electron diffraction (LEED) measurements were performed in the third one, the NanoESCA end-station of ELI - ALPS. The STM and the XPS-LEIS systems has been described previously [24].

In the STM chamber the STM head was controlled by a commercial SPM electronics (MK2-A810 and MK3Pro-HV1 produced by SOFT-dB) and by GXSM-Linux software. STM images recorded in constant current mode were taken up at a bias of −1 V (on the sample) and a tunneling current of 1nA. The W-tip was conditioned by voltage pulses (+3 V, 10nA). Some of the images were gently smoothed by fast Fourier-transformation (FFT). The distances on STM images were calibrated by measuring the unit cell sizes and the atomic step height on $TiO_2(1 1 0)-$ (1 × 1) sample (0.296 nm × 0.650 nm, 0.297 nm). The following nearest atom–atom distances were used during data evaluation: Rh (0.2687 nm), Au (0.2884 nm). Concerning the determination of the size (height, diameter and volume) of the 3D particles (which have larger height than 0.5 nm) and their lateral concentration, we took into account the rather inhomogeneous particle-position and the wide particle-size distribution, moreover the tip-shape effects. Regarding some subjective factors in this job, we can state that the accuracy of these particle-characteristics given in this work is not better than ±10 %.

In the XPS-LEIS chamber an Al K_α X-ray source [58] was applied for XPS, performed with constant pass energy, and at a detection angle of 16° with respect to the surface normal. The binding energy scale, referenced to the Fermi level, was calibrated by fixing the Au $4f_{7/2}$ peak of bulk gold to 84.0 eV and the Rh $3d_{5/2}$ peak of the bulk Rh to 307.2 eV. For LEIS, 800 eV helium ions were applied at a low ion flux (~0.03 μA/ cm^2). The scattering angle was 95°. The sample temperature was measured with a chromel–alumel (K-type) thermocouple spot-welded to the sample.

The NanoESCA end-station of ELI ALPS consists of a preparation chamber (1 × 10^{-10} mbar) and an analysis chamber (3 × 10^{-11} mbar). LEED measurements were performed in the preparation chamber applying a 4-grid rear view LEED of OCI Vacuum Microengineering.

In all chambers, one side polished Rh(1 1 1) single crystals (orientation accuracy: better than 0.1°) were used. The samples were cleaned

according to the following recipe: cycles of Ar$^+$ ion sputtering for 20 min (1.5 keV) at 300 K and annealing in UHV at 1200 K for 10 min. The sample was then annealed in 3×10^{-8} mbar O_2 at 1050 K for 30 min. The final step was annealing in UHV at 1250 K for 1 min. h-BN over-layers were synthetized via the thermal decomposition of borazine at 1000–1050 K, Borazine (purity: greater than 99.8 %) was produced by Katchem Ltd. High-purity (99.95 %) Au was deposited by commercial e-beam heated PVD sources. The coverage of Au is expressed in equivalent monolayers (ML), defined as the surface concentration of rhodium atoms in the topmost layer of Rh(1 1 1): 1.60×10^{15} cm^{-2}. This defini-tion is justified by the pseudomorphic growth of Au on Rh(1 1 1) up to 1 ML [56]. In the XPS-LEIS chamber, a quartz crystal microbalance (QCM) was applied to adjust the evaporation rate, while in the STM chamber gold coverage was deduced from the volume of the deposited gold nanoparticles. In both cases, the evaporation rate was ~0.2 ML/min. In order to assess our relative LEIS sensitivity for Au and Rh, we have to take into account that in our setup the Au LEIS peak intensity of a thick (5 ML) continuous gold film on Rh(1 1 1) is 90 % of the clean Rh(1 1 1) intensity. Considering that the topmost layer atomic distances of the thick film is close to that of Au(1 1 1) [56], and the packing densities of Au(1 1 1) and Rh(1 1 1) are 1.39×10^{15} cm^{-2} and 1.60×10^{15} cm^{-2}, respectively, the *per ML* relative sensitivities for Au and Rh are equal with a precision of 3.5 %, since we fixed the Au ML definition to the Rh (1 1 1) packing density. For this reason the Au LEIS intensities are shown normalized to the clean Rh(1 1 1) LEIS intensity.

For DFT calculations the Vienna Ab initio Simulation Package (VASP) [59,60] with the projector augmented wave method [61] and van der Waals correction (optB86b) [62,63] were employed. To contribute to the understanding of the experimental observations we modeled different systems: (i) h-BN on metal substrate, h-BN/Rh(1 1 1) and h-BN/Au/Rh(1 1 1), (ii) monolayer metal (Rh and Au) on h-BN/Rh (1 1 1), (iii) Rh and Au adatom adsorption on flat free-standing h-BN considering various defect sites in the h-BN layer, (iv) Rh and Au adatom adsorption on h-BN/Rh(1 1 1), (v) Rh and Au adatom intercalated below the nanomesh h-BN layer on Rh(1 1 1), and (vi) 19-atoms clusters of Rh and Au [53] in the pore of h-BN/Rh(1 1 1). For flat h-BN (iii) a 7×7 BN layer ($a_{2D} = 0.248$ nm) is considered: either defect-free intact h-BN, or with the following defects: single B vacancy (V_B), single N vacancy (V_N), and BN double vacancy (V_{BN}), and metal adatoms were added to sys-tematically varied positions. Where a metal support is present (i,ii,iv,v, vi), the $(13 \times 13$ BN$)/(12 \times 12$ Rh$)$ superstructure [31] with the experimental lattice constant of Rh, $a_{2D} = 0.269$ nm was adapted. Here, the slab geometry in the supercell is always based on at least two Rh layers (followed by another metal layer and h-BN (i), or h-BN and metal layer (ii), and adding metal atoms to various positions (iv,v,vi)) from which the bottom Rh layer was fixed and the rest of the atoms were relaxed to determine their equilibrium geometry with a force criterion of 0.2 eV/nm. The Brillouin zone was always sampled by the Γ point only.

3. Results and discussion

3.1. Characterization of the h-BN covered Rh(1 1 1) surface

First, the surface structure was characterized by LEED. Diffraction patterns obtained at a primary energy of 62 eV are depicted in Fig. 1. LEED images of clean Rh(1 1 1) and h-BN covered Rh(1 1 1) are also shown (A and B, respectively). For Rh(1 1 1) six spots with threefold symmetry were observed, as expected. The lattice constant of Rh(1 1 1) is 0.269 nm at room temperature [64]. The preparation of the nanomesh on Rh(1 1 1) resulted in a new set of bright spots at a somewhat larger distance from the center, assigned to the h-BN lattice with a slightly smaller lattice constant of 0.248 nm (Fig. 1B). The main spot to spot distances for Rh(1 1 1) were smaller by 7.9 % than the spot to spot dis-tances for h-BN, implying a ratio of 0.921 for the lattice constants of h-BN and Rh(1 1 1). The satellite points in hexagonal arrangement around the main diffraction dots reflect the appearance of the well-known
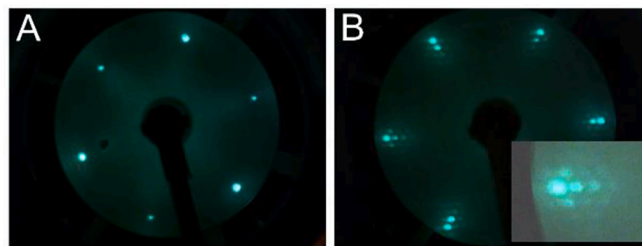
Fig. 1. LEED patterns recorded with a primary energy of 62 eV on (A) clean Rh (1 1 1), and (B) h-BN covered Rh(1 1 1). The insert in B exhibits a magnified dot region.

nanomesh superlattice with a periodicity of ~3.2 nm (Fig. 1B inset). This is in accordance with the 13 over 12 superstructure reported in literature [9,24,31,65].

The surface structure was followed also by STM (Fig. 2). The h-BN supported by Rh(1 1 1) shows the typical hexagonal nanomesh period-icity of 3.2 nm after its fabrication at 1050 K (Fig. 2A). In the left bottom of this image a high-resolution image can be seen, where the hexagonal periodicity of 0.25 nm is characteristic of the next neighbor distance of BN-rings (unit cell). This structure remains stable after the 5 min annealing at 1175 K (B). Note that the different pore-wire contrast is a typical feature and purely due to the different tip-state and imaging parameters [49]. A dramatic change appears in the morphology after annealing at 1200 K (C). Although the atomic step line of Rh(1 1 1) surface is clearly visible diagonally on the image, the nanomesh struc-ture disappeared and the atomic terraces exhibit a rather disturbed morphology. Let us note that in some cases we recorded also ordered nanomesh structure at this temperature. Nevertheless, annealing at 1225 K resulted in a total disappearance of the nanomesh texture and the hole formation on the terraces continued (Fig. 2D). An interesting image of 5×3 nm^2 is inserted in D, which was recorded on a flat region showing a quadratic symmetry with a periodicity of 0.34–0.36 nm. This side-feature may result from the formation of a reconstructed Rh lattice induced by built-in B atoms originating from the decomposition of BN layer, but neither the formation of cubic BN can be excluded. Further studies are needed for a clear assignment. In summary, these STM re-sults, in accordance with LEIS results presented below, show that the h-BN monolayer supported on Rh(1 1 1) is stable approximately up to 1175 K. Concerning the thermally induced decomposition of metal supported h-BN, previous studies revealed a thermal stability up to 1275 K for h-BN/Ru(0001) and 1223 K for h-BN/Ir(1 1 1), respectively [13,35]. The onset of h-BN degradation on Rh(1 1 1) as a gradual disappearance of h-BN regions in STM was reported to be 1160 K [18], in accordance with our present and recent study [24].

3.2. Metal deposition at 300 K and the effect of subsequent annealing

As a next step, one monolayer of rhodium was deposited at room temperature on h-BN covered Rh(1 1 1), followed by subsequent annealing at stepwise increased temperatures for 5 min. After each annealing step, LEIS spectra were collected near 300 K (Fig. 3A). Please note that LEIS provides information almost exclusively about the outermost atomic layer, when noble gas ions are applied [66]. No Rh LEIS peak was found after the h-BN synthesis, which confirmed the continuity of the h-BN monolayer. The Rh signal obtained after depo-sition at 300 K gradually attenuated due to annealing, and almost dis-appeared at 950 K. However, at higher temperatures, the Rh peak reappeared. The inset of Fig. 3A allows an estimation of our detection limit for Rh. After h-BN synthesis, a broad peak has been observed centered at lower kinetic energies compared to the Rh peak. This is assigned to backscattering in deeper layers and reionization [66]. This peak can be used as a baseline, when quantifying Rh in the outermost atomic layer. The small Rh peak after metal deposition and annealing at
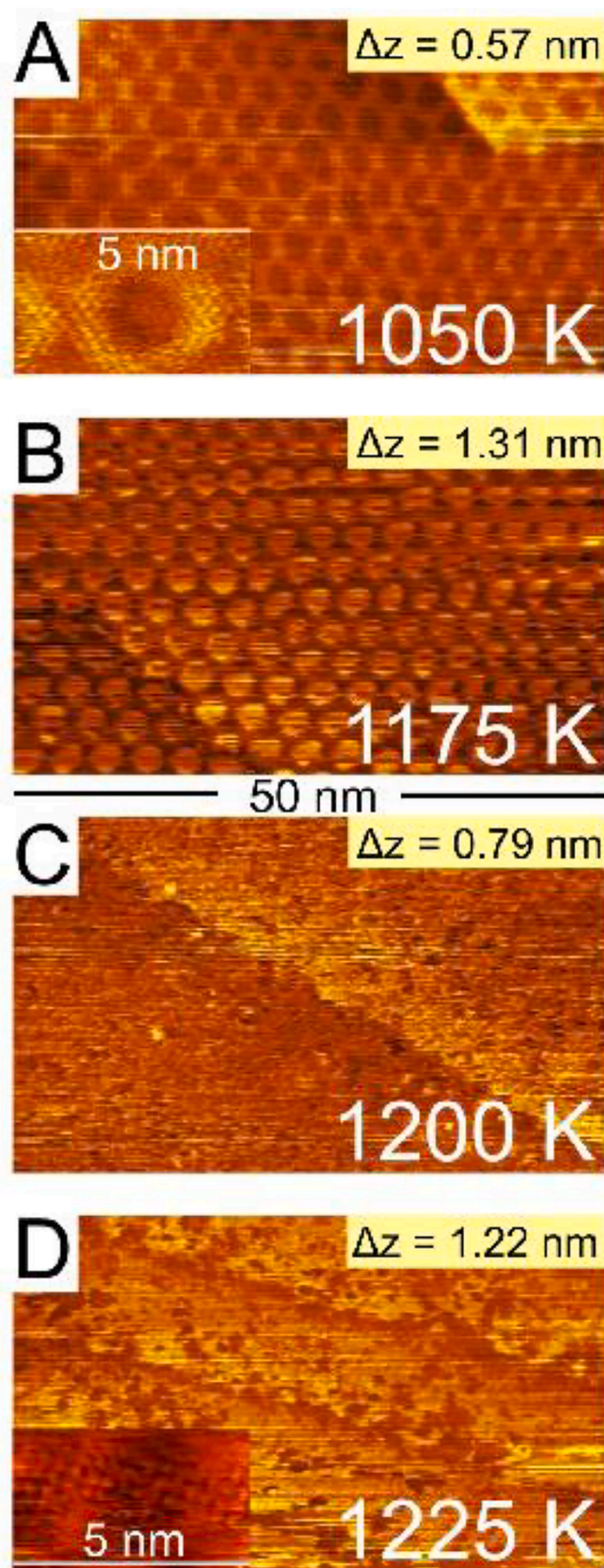
Fig. 2. STM images of 50×30 nm^2 recorded on (A) a h-BN nanomesh covered Rh(1 1 1) surface, followed by 5 min annealing at higher temperatures: (B) 1175 K, (C) 1200 K, (D) 1225 K. The inserted high resolution image of 5×3 nm^2 (left bottom in A) exhibits the h-BN lattice itself.

950 K corresponds to 0.004 ML of Rh. From the figure, it can be inferred that our detection limit for Rh is ~0.002 ML. Since our LEIS sensitivity for Au is nearly the same as for Rh, the detection limit of Au is also ~0.002 ML. The same experiment was repeated with different amounts of Rh deposited. The Rh peak intensities observed after gradual annealing are displayed in Fig. 3B, normalized to the LEIS intensity of clean Rh(1 1 1). Please note that for the rhodium intensity no neutralization matrix effects take place in the combined rhodium–boron nitride system [24]. The B and N LEIS peaks of the nitride were very weak, close to our detection limit, in accordance with literature data, which can be explained by the lower sensitivity of LEIS for light elements [7,24].

At nearly all initial coverages, a mild annealing up to ~500 K resulted in an increase in the Rh intensity, which is assigned to the desorption of background gases (CO, H$_2$, H$_2$O, …). Thereafter, normalized Rh intensity was much smaller than the amount of Rh deposited (in ML), revealing the presence of 3D nanoparticles (Volmer-Weber growth mode). *At small and medium coverages up to 1 ML,* further annealing led to gradual attenuation and to the (nearly) complete disappearance of the rhodium signal by ~950 K. The absence of the Rh LEIS peak is a clear sign for the disappearance of rhodium from the topmost atomic layer, e. g. by intercalation. Other possible channels are the agglomeration (sintering) and desorption of Rh. Agglomeration, however, cannot lead to the complete disappearance of the Rh peak. While desorption can indeed contribute to the intensity loss, it is not straightforward to quantify this effect. It seems reasonable to assume that Rh desorption has a larger activation energy than Au desorption, because the bulk melting and boiling points of gold are smaller, and Rh interacts more strongly with h-BN than Au. Based on the comparison of XPS and LEIS results obtained after the deposition and thermal annealing of Au on h-BN/Rh(1 1 1) it was estimated that not more than 44 % of gold desorbed up to 1050 K at $\Theta_{Au} \leq 1$ ML, therefore the majority of Au intercalated [24]. Consequently, we feel safe to conclude that in the present case the desorption of Rh is not the majority net process up to 1050 K at $\Theta_{Rh} \leq 1$ ML. *At larger initial Rh coverages* ($\Theta_{Rh} \geq 5$ ML), the Rh LEIS peak did not disappear at any temperatures, indicating there is always some Rh in the outermost atomic layer. Due to the strong 3D character of the growth, a continuous Rh film was formed only at $\Theta_{Rh} = 50$ ML, where normalized Rh LEIS intensity reached 1 (not shown).

Concerning the behavior at high temperatures, at each coverage, a sharp rise/reappearance of the Rh intensity was observed at 1150–1200 K, which is attributed to the opening/disruption of h-BN film (Fig. 3B,C). Even at zero or low initial Rh coverages, ~20 % of the surface becomes uncovered after 5 min annealing at 1200 K, in accordance with the STM results shown in Fig. 2.

Turning on the behavior of gold deposits, we first present LEIS results obtained after the deposition and subsequent annealing of Au on h-BN/Rh(1 1 1). While in our previous study [24] we dealt with low and moderate gold coverages, here we present results on a broad coverage range from 0.08 ML to 10 ML (Fig. 3D–F), and a comparison will be made with the Rh/h-BN/Rh(1 1 1) system presented above. Gold LEIS intensities are normalized to the rhodium intensity of clean Rh(1 1 1). It is known that gold follows a Volmer-Weber growth mode at 300 K except for very low coverages [24,43,45], which is confirmed again by the present experiments. 10 ML of Au was not sufficient to form a continuous film. Since Au is not subject to background gas adsorption at room temperature [44], mild annealing in the range of 300–700 K did not induce any increase in the Au LEIS intensity, in contrast to Rh, but the Au LEIS peak gradually attenuated (Fig. 3D). At around 750 K, a sharp decrease set in for larger coverages. In the range of 800–1050 K a slower attenuation took place (similarly to Rh). A notable difference between Au and Rh is that the gold signal was completely suppressed at high temperatures (~1000–1100 K) at any initial Au coverages up to 10 ML, which clearly demonstrates intercalation even for large gold doses. Sintering and desorption also influence LEIS intensity. Starting with 10 ML of Au on h-BN/Rh(1 1 1), XPS data indicated the presence of ~4 ML of Au between h-BN and Rh(1 1 1) after intercalation (the rest desorbed),
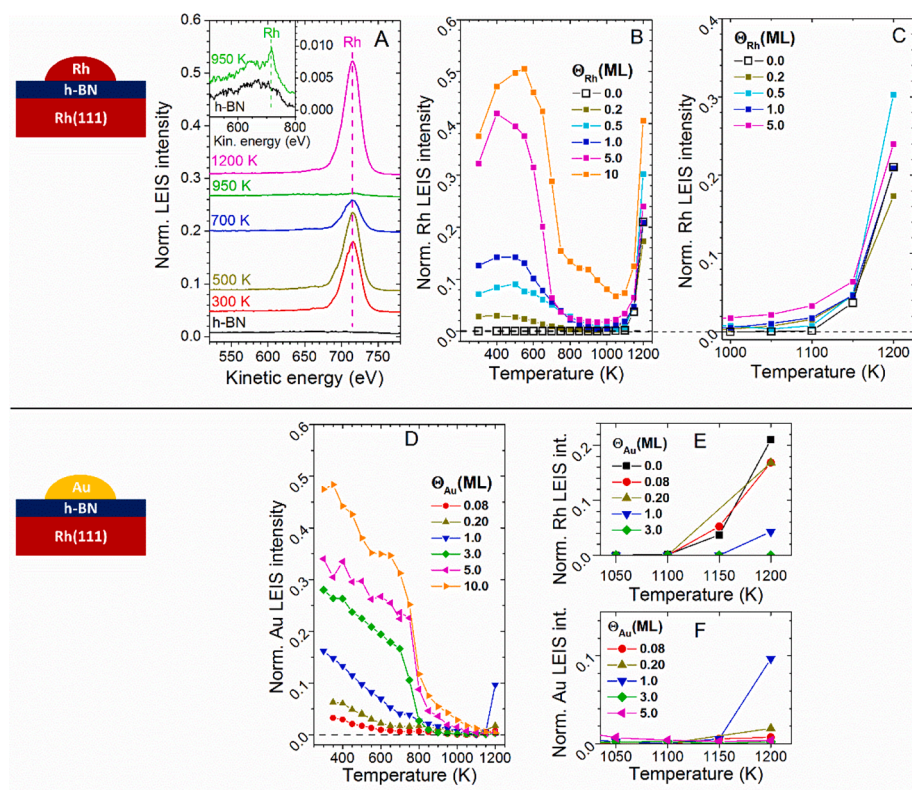
Fig. 3. LEIS results about metal deposition on h-BN/Rh(1 1 1) at 300 K, followed by annealing treatments for 5 min. (A) LEIS spectra after 1 ML Rh deposition and annealing. For comparison, the LEIS spectrum of the h-BN covered Rh(1 1 1) surface is also shown. inset: magnified spectra of h-BN/Rh(1 1 1) and after 1 ML Rh deposition and annealing at 950 K. (B) Rh peak intensities obtained with different amounts of rhodium dosed on h-BN/Rh(1 1 1). (C) A selection of experiments presented in (B) zooming in the high temperature region. (D) Au intensities obtained after gold deposition and annealing. (E, F) Rh and Au intensities, obtained in a selection of measurements presented in (D) zooming in the high temperature region. (B-F) LEIS intensities are normalized to the Rh intensity of the clean Rh(1 1 1) surface. The sketches on the left serve only to display the sequence of layers after the metal deposition step.

applying Scofield photoelectric cross sections [67] and inelastic mean free path values of Tanuma, Powell and Penn [68]. In the model for XPS quantification, it was assumed that Rh bulk does not contain any gold, because of the very low solubility of Au in Rh.

For the initial gold coverage range of 0.08 ML–5 ML, the high temperature region of Fig. 3D is presented magnified in Fig. 3F, while normalized Rh intensities from the same experiments are shown in Fig. 3E. The reappearance of Rh and Au intensities indicates the opening/decomposition of the h-BN monolayer at 1150–1200 K. With increasing initial gold content, the Rh intensity observed at 1200 K gradually decreases, and completely disappears at $\Theta_{Au} = 3$ ML and above. At the same time, the dewetting of h-BN results in increasing Au intensities up to $\Theta_{Au} = 1$ ML, because the opening of the nanomesh liberates Au coated Rh(1 1 1) areas. Please note that the desorption of gold from Rh(1 1 1) is rather fast at 1200 K, as will be discussed about Fig. 7, which attenuates the observed gold LEIS intensity. A further increase in the initial gold content to 3 ML or above completely suppresses the disruption of h-BN, which reveals a substantial stabilizing effect of gold (Fig. 3D–F). Since intercalation is complete by ~1050 K, gold atoms separate rhodium from boron nitride. The h-BN layer remains intact, because the chemical reactivity of the smooth interfacial gold layer is much weaker than that of rhodium. On the other side, this observation reveals that the chemical activity of Rh plays an important role in the high temperature reopening/disruption of the h-BN nanomesh on Rh (1 1 1); rhodium catalyzes the rupture of covalent B–N bonds, most probably in the pore regions, where the rhodium–nitride distance is smaller, and electronic hybridization is stronger.

Before the presentation of complementary STM investigations, let us recall several main characteristics perceptible in Fig. 3. The measurement series with both Rh and Au show similar tendencies, but also notable differences, which are particularly well seen for the higher coverages above 1 ML. Four characteristic temperature ranges can be identified. T-Range I: at relatively low temperatures (for Rh between 300 K and 550 K, for Au between 300 K and 700 K) a gradual and slow attenuation takes place due to a thermally activated sintering of the

metal deposit as described above. In the case of Rh, the slight enhancement of the signal between 300 K and 500 K is probably originated from the desorption of contaminants. T-Range II: the metal LEIS signal decreases steeply between 600 K and 750 K for Rh, and between 700 K and 850 K for gold. This indicates that not only the sintering mentioned above takes place, but probably a new surface process sets in (see below at the evaluation of STM measurements). Interestingly, this process requires a higher activation energy for gold. T-Range III: annealing further (up to ~950 K for Rh, and 1050 K–1100 K for Au) the metal signal gradually vanishes, with the exception of higher Rh coverages. T-Range IV: in the highest temperature range from ~1150 K the LEIS metal signals start to increase intensely due to the disruption of h-BN, which is suppressed at higher gold doses.

In Fig. 4 two series of the most characteristic STM morphology images (chosen from at least 9–10 other ones recorded at the different sites of the sample) are presented in order to compare the thermal stability of Rh and Au deposits and to disclose more details of the thermally activated processes. In both cases, we dosed approximately 6 ML (±10 %) initial coverage. The coverage of metal deposits was calculated from the total volume of 3D nanoparticles formed at 300 K (A1, B1) or visible as 3D nanoparticles after the annealing at higher temperatures (A2-A7 and B2-B7). Note, 3D nanoparticles were defined in this case as particles higher than 0.5 nm (see above). This coverage value does not imply the full amount of admetals present on the surface, especially at higher temperatures. Taken the specific images from Fig. 4, the characteristic parameters like (A) average particle diameter, (B) average height, (C) total amount of 3D nanoparticles expressed in ML, (D) occupancy in percentage (the surface area covered by nanoparticles relative to the total substrate surface area) and (E) surface concentration of the 3D nanoparticles (particle density) are shown in Fig. 5.

By checking both the images and the calculated parameters, the Volmer-Weber growth mode for both metals at room temperature is confirmed, in accordance with LEIS. It can be clearly seen that between 300 K and 650 K the average diameter gradually increases from 5 nm up to 6.5 nm and from 9 nm up to 10.5 nm for Rh and Au, respectively
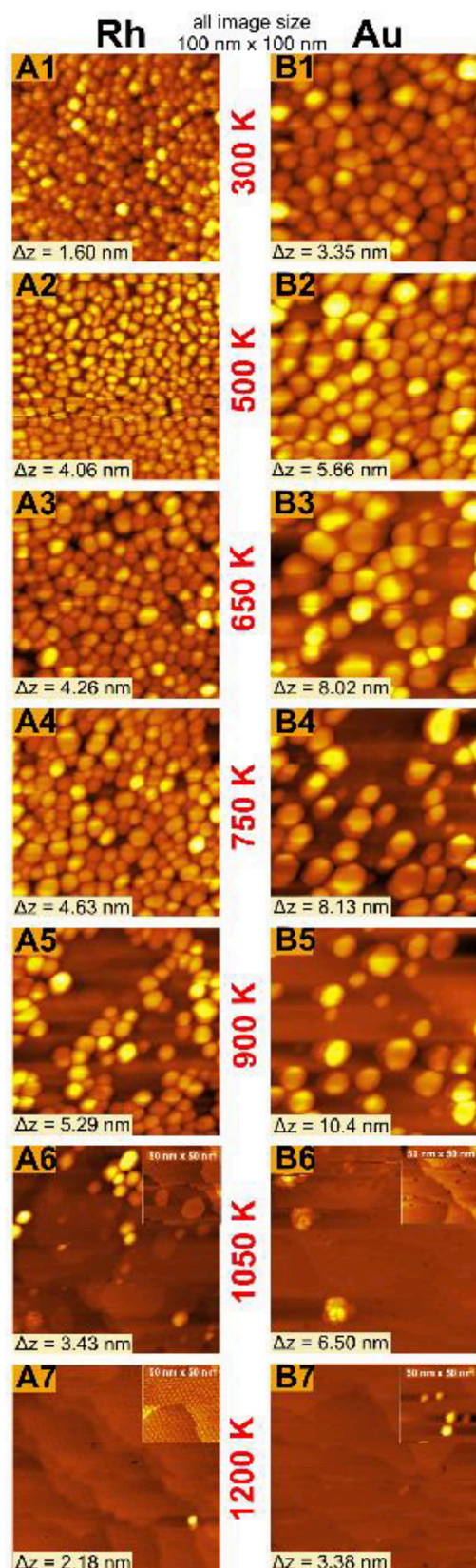
Fig. 4. STM images of 100×100 nm^2 taken on Rh(1 1 1) covered by h-BN, and exposed to approximately 6 ML of (A1) Rh or (B1) Au, followed by 5 min annealing at higher temperatures: (A2, B2) 500 K, (A3, B3) 650 K, (A4, B4) 750 K, (A5, B5) 900 K, (A6, B6) 1050 K and (A7, B7) 1200 K. The insets of 50×50 nm^2 in A6, B6, A7, B7 exhibit special regions of the surface.

(Fig. 4A1–A3, B1–B3, and Fig. 5). The larger particle size of Au detected already at 300 K indicates obviously a larger diffusion ability and a smaller nucleation probability of Au on h-BN compared to Rh. Regarding the average height, in the case of Rh there is only a little increase from 1.3 nm up to 1.5 nm, while in the case of Au there is a gradual and significant enhancement from 1 nm up to 2.8 nm. In this temperature range, the total volume of the 3D particles does not change and only a moderate change can be observed for the occupancy. The particle density gradually decreases from 3×10^{12} to 1.8×10^{12} cm^{-2} (Rh) and from 1.0×10^{12} to 0.4×10^{12} cm^{-2} (Au). All these morphological changes demonstrate the occurrence of thermally activated Ostwald ripening as it was also deduced from the LEIS measurements for T-Range I (300 K–550 K for Rh, and 300 K–700 K for Au).

It is a much more surprising observation that in T-Range II (600 K – 750 K for Rh, and 700 K–850 K for Au), where a rather sharp decrease in the metal signal intensity was detected by LEIS (Fig. 3B, D), there are only little changes in the particle parameters for Rh, depicted in Fig. 5, while for Au the decrease in 3D amount and occupancy are more significant. This fact clearly reveals that beside the slow Ostwald ripening there exist different process(es) resulting in the radical decrease in LEIS signals, and these can be different for Rh and Au. As Rh has little change in 3D volume and occupancy, intercalation cannot fully explain the observed behavior. A reasonable explanation is that the decomposed components of h-BN migrate on the top of supported particles in this temperature range. The presence of an h-BN overlayer on top of Rh after 700 K annealing has been demonstrated also by sputter depth profiling, as explained in the Supplementary material. This process is probably similar to the decoration/encapsulation phenomenon, which takes place frequently on metal nanoparticles supported by reducible oxides [69,70]. It is important to mention here that the comparison of STM and LEIS results is not biased by possible differences in the temperature measurement in the two chambers. According to a cross-calibration with a pyrometer, the difference between the two temperature scales is <20 K. Here we emphasize that although the 3D shape of the metal nanoparticles, which is a sort of surface roughness, leads to an underestimation of the metal covered surface fraction based on LEIS intensities, it does not influence the conclusion about encapsulation. According to our STM results (Fig. 5), the average Rh cluster height is quite stable up to T-Range II, while the diameter increases, implying that the 3D Rh nanoparticles actually become flatter, which cannot lead to a loss of Rh LEIS intensity. The encapsulation of metal nanoparticles by BN fragments requires the rupture of BN bonds in the original nanomesh by metal clusters. Since the reactivity of Rh is stronger than that of gold, this process is more specific to rhodium. Please note that the rupture of B–N bonds in borazine during h-BN growth on Rh(1 1 1) was also postulated [18], and Rh clusters are even more reactive than the flat Rh(1 1 1) surface. Encapsulation, however, does not exclude intercalation (diffusion of metal atoms below h-BN), but may promote it: the defect sites created in h-BN can serve as intercalation channels. Regarding the atomic mechanism of encapsulation, it needs further studies to disclose, whether it proceeds via diffusion of BN fragments or B, N atoms on the surface of Rh nanoparticles, or via diffusion of B and N atoms through the bulk of Rh clusters. It is also to be noted that the reactivity of gold depends sensitively on its cluster size [71]. Therefore, while the encapsulation process is not salient for the 6 ML Au case, we cannot exclude it becomes more facile for small Au nanoparticles. Similarly, although we demonstrated this phenomenon at large rhodium doses, it seems reasonable to assume that it takes place for small Rh coverages as well.

A further temperature rise up to 1050 K (~T-Range III) results in a gradual attenuation in the 3D particle concentration, accompanied by the decrease in the occupancy and the total volume of the 3D nanoparticles (Fig. 4A4–A7, B4–B7 and Fig. 5C, D, E). In accordance with the conclusions deduced from LEIS measurements, for gold a main process in this temperature range is the gradual intercalation of the deposited metal, but desorption is also significant, as mentioned above. In the case
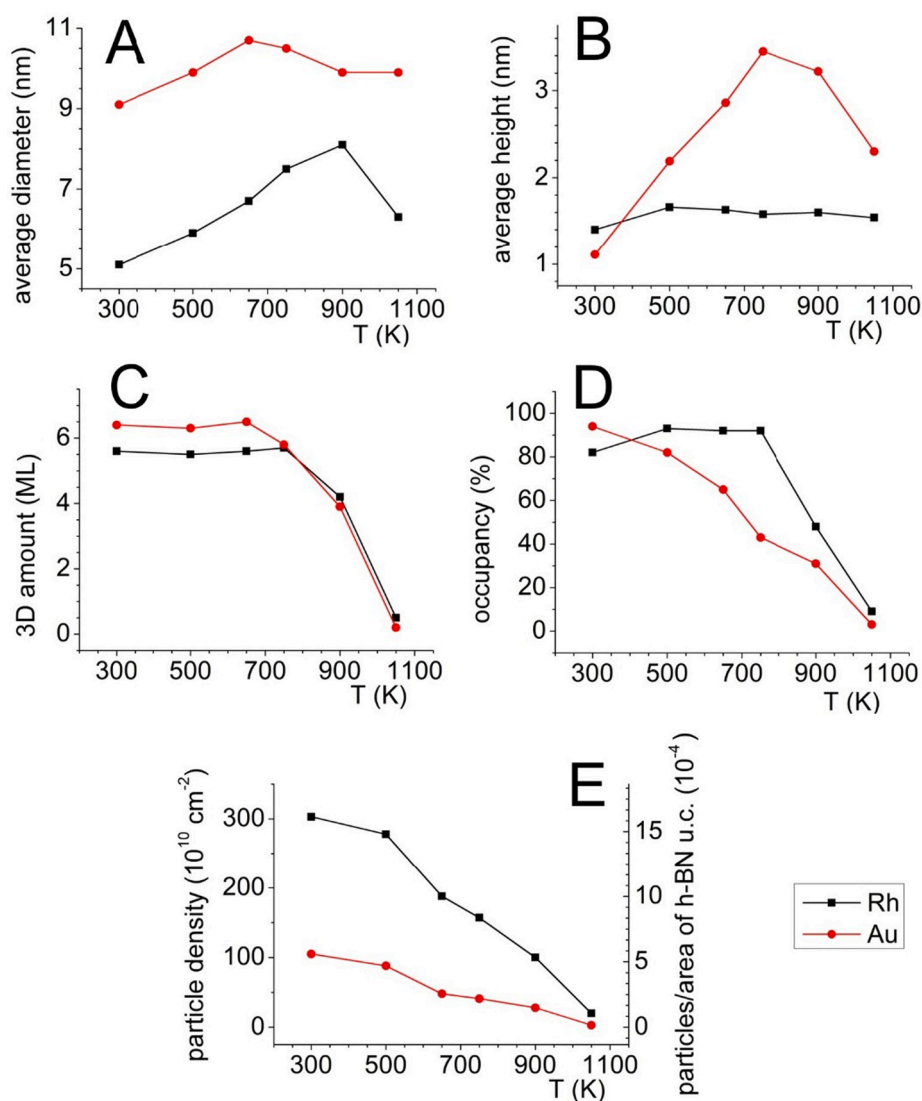
Fig. 5. Characteristic parameters of the 3D nanoparticles calculated on the basis of STM images in Fig. 4 and plotted as a funtion of temperature.
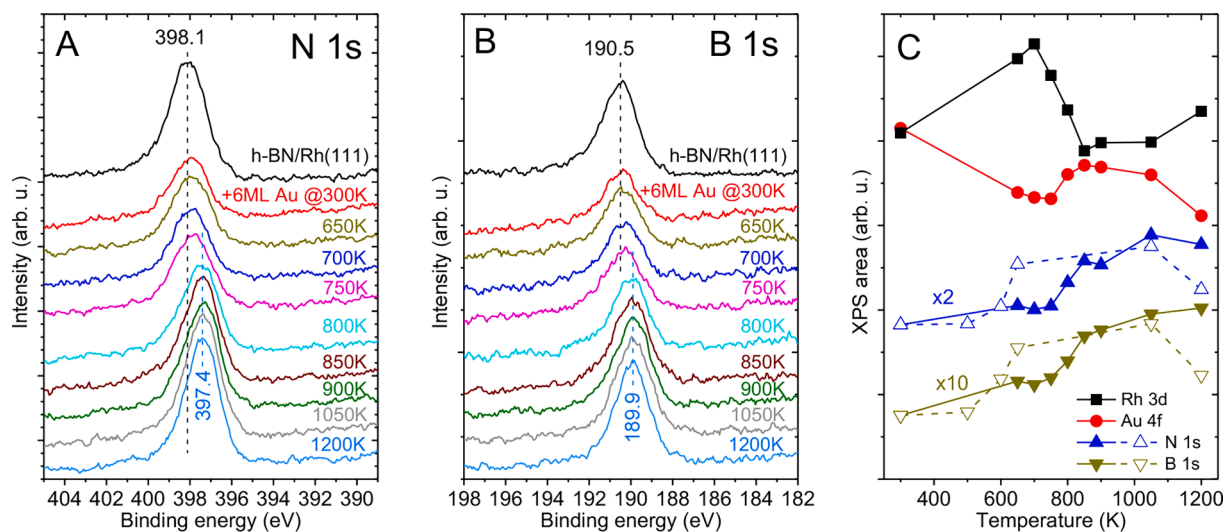

Fig. 6. (A) N 1s and (B) B 1s XPS regions of h-BN/Rh(1 1 1), and those obtained after the deposition of 6 ML Au on h-BN/Rh(1 1 1) at 300 K, followed by annealing at increasing temperatures for 5 min. (C) XPS areas for the Rh 3d, Au 4f, N 1s and B 1s regions (filled symbols) obtained in the measurement described for (A) and (B). For comparison, we displayed also N 1s and B 1s areas obtained after the deposition of 6 ML Rh on h-BN/Rh(1 1 1) at 300 K, followed by annealing at increasing temperatures for 5 min (empty symbols).

of Rh, a flattening of encapsulated metal clusters take place, and atoms can detach from encapsulated clusters and diffuse below h-BN to step edges of the substrate or to other 2D Rh islands (2D sintering), further reducing the 3D volume in STM. Intercalated gold atoms also diffuse to substrate steps. Some important details appear also on the images recorded after annealing up to these temperatures (Fig. 4A5–A7, B5–B7). For the Rh deposit, the inserted image of 50×50 nm^2 clearly shows the appearance of monolayer thick 2D hexagonal particles, which are certainly intercalated Rh particles underneath the h-BN net (Fig. 5A6). Fig. 4B6 does not show similar 2D particles for Au, probably because of the faster diffusion and attachment of the intercalated Au atoms to Rh steps. After the highest annealing treatment (at 1200 K) the 3D nanoparticles almost disappeared in both cases, at the same time a complete nanomesh structure is visible again for the Rh deposit, but in the case of Au there is no nanomesh formation due to the intercalated Au layers, as it was expected. Since bulk Au and Rh are practically immiscible [57], the diffusion of Au to deeper layers of Rh(111) is very limited, and the gold-rhodium interface is rather sharp.

The growth and thermal properties of Au on h-BN/Rh(111) were also studied by XPS. 6 ML of Au was deposited on h-BN/Rh(111) at 300 K, and the surface was annealed to higher temperatures for 5 min. N 1s and B 1s XPS spectra are shown in Fig. 6A and B, respectively. XPS peak areas are collected in Fig. 6C. After h-BN synthesis, the N 1s peak was observed at 398.1 eV, while the B 1s peak at 190.5 eV, in accordance with the literature [24,43,46]. The pore-wire duality of nanomesh induces an asymmetry of the peaks toward higher binding energies. The deposition of gold resulted in a small ~0.15 eV shift of peak positions toward lower binding energies. Annealing up to 700 K (T-Range I) led to a small increase in B 1s, N 1s, and Rh 3d peak areas, attributed to sintering. The change in Rh 3d area might seem more significant, but its enhancement up to 700 K corresponds only to ~10 % of Rh 3d area for h-BN/Rh(111). Between 700 K and 850 K (T-Range II) steeper changes took place: an increase in N 1s, B 1s and Au 4f areas, accompanied by an attenuation of Rh 3d area. At the same time, we observed an additional ~0.5 eV shift in N 1s and B 1s positions toward lower binding energies. The enlargement of nitrogen and boron peaks is compatible with both encapsulation and intercalation of gold as discussed about LEIS and STM data above. However, the enhancement of Au 4f area, accompanied by the loss of Rh 3d area cannot be explained by encapsulation itself, sintering or desorption, because these processes result in an opposite change. On the other hand, the intercalation of gold is compatible with this observation: although during intercalation gold atoms get covered by h-BN, the intercalated gold is two dimensional (attached to Rh(111) step edges), therefore gold atoms will not shadow each other anymore, but will shadow the Rh(111) substrate more efficiently. More precisely, we propose that in this temperature range both sintering and intercalation proceed to some extent, but intercalation is the dominant process. The downward shift of B 1s and N 1s peaks is explained by the presence of Au at the h-BN/Rh(111) interface [24]. In T-Range III from 850 K to 1050 K only minor changes were found. However, annealing to 1200 K led to a drop of Au 4f area, an increase in Rh 3d area, while N 1s and B 1s areas did not change appreciably. We attribute this change to the desorption of some gold before complete intercalation. In this measurement, the Au LEIS intensity was also monitored simultaneously, and the disappearance of gold from the outermost layer was complete only at 1150 K. An analogue XPS experiment was also performed, in which 6 ML of Rh was deposited on h-BN/Rh(111), followed by subsequent stepwise annealing. No significant changes in the N 1s and B 1s peak shapes were observed (not shown). The obtained N 1s and B 1s peak areas are displayed in Fig. 6C, for comparison. In accordance with LEIS results presented above, the steep change (increase) in these areas (empty symbols) arose at smaller temperatures (~600 K) when compared to the Au/h-BN/Rh(111) experiment (filled symbols). This sudden increase is mostly attributed to the encapsulation of Rh nanoparticles by BN. The loss of N 1s and B 1s areas at 1200 K is due to the decomposition of BN at this temperature.

As mentioned above, we assume that gold can stabilize the h-BN monolayer, because it separates h-BN from the more reactive rhodium. In this picture, the gold layer itself has to be stable at the interface at 1200 K even for longer times. This is not a trivial requirement, since the diffusion of gold on h-BN is relatively fast even at lower temperatures, leading to intercalation. Besides, it has been reported that intercalated Mn diffused back onto h-BN surface and desorbed at 773 K [42]. Therefore, the amount of gold under h-BN was monitored by XPS as a function of time at 1200 K (Fig. 7). In this experiment, 10 ML of Au was deposited on h-BN/Rh(111) at 300 K, and it was intercalated by annealing up to 1200 K. Intercalation was monitored by LEIS, and time zero of Fig. 7 is defined as the moment when complete intercalation was reached. At t = 0 min, XPS areas indicated that 4 ML of Au was present below h-BN. Au 4f and Rh 3d XPS areas are shown in Fig. 7 as a function of additional heat treatments at 1200 K. XPS spectra were collected near 300 K after the respective annealing treatments. As it is demonstrated by the figure (filled symbols), both Au 4f and Rh 3d peak areas stayed remarkably stable for 60 min at 1200 K, the drop in Au 4f area was only 4 %. This experiment also confirmed that the diffusion of gold toward rhodium bulk is not significant, in accordance with the bulk immiscibility of these metals.

For comparison, we also performed a similar measurement in the absence of h-BN. In this case 3.65 ML of Au was deposited on Rh(111) at 500 K, followed by 5 min annealing at 1050 K. This resulted in a smooth film without gold desorption. The surface was then annealed at 1200 K for increasing times, and Au 4f and Rh 3d regions were collected near 300 K after each annealing treatment. The obtained peak areas are displayed in Fig. 7 with open symbols. Gold evaporation was substantial already after 5 min at 1200 K, and desorption was nearly complete after 15 min. This comparison reveals the decisive role of the nitride monolayer in keeping gold at the interface. On the other hand, gold at the interface keeps h-BN tightly closed.

3.3. Variation of the deposition temperature

We also studied the effect of the deposition temperature in the range of 300–600 K. Increasing amounts of gold were evaporated on h-BN/Rh(111) at 300 K and 400 K substrate temperatures, monitored by XPS and LEIS (Fig. 8). The Au 4f areas as a function of gold coverage (in this case
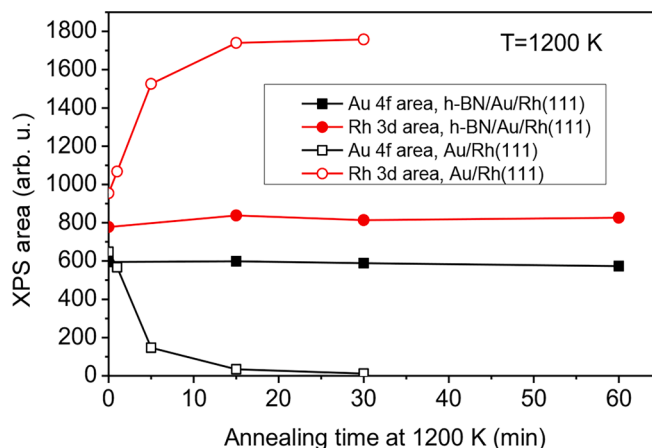

Fig. 7. Au 4f and Rh 3d XPS areas obtained after annealing at 1200 K for increasing times. **Filled symbols:** h-BN/4 ML Au/Rh(111) prepared by the deposition of 10 ML of Au on h-BN/Rh(111) at 300 K; followed by annealing up to 1200 K until complete intercalation is reached as monitored by LEIS. t = 0 min for the experiment is defined as the moment, when complete intercalation is achieved. Due to desorption during intercalation, the gold coverage was 4 ML at t = 0 min. **Empty symbols:** 3.65 ML Au/Rh(111) obtained by Au deposition on Rh(111) at 500 K, followed by 5 min annealing at 1050 K. t = 0 min is defined in this case as the end of annealing at 1050 K. In all cases, XPS spectra were obtained near 300 K after the respective heat treatments.
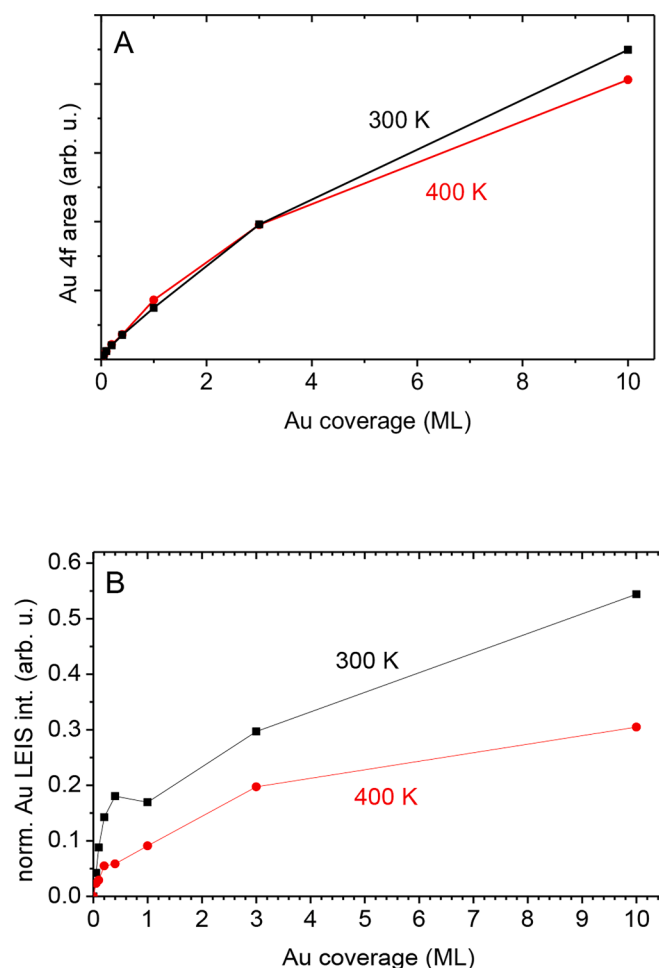
Fig. 8. (A) The Au 4f XPS area obtained during deposition of Au on h-BN/Rh (1 1 1) at 300 K and 400 K. (B) Au LEIS intensity normalized to the Rh intensity of the clean Rh(1 1 1) surface obtained during deposition of Au on h-BN/Rh (1 1 1) at 300 K and 400 K.

gold coverage means gold exposure) were nearly identical for the two temperatures (Fig. 8A), indicating that the sticking coefficient (S) was also identical, implying S = 1. However, we detected a significant difference in Au LEIS intensities (Fig. 8B).

At 400 K much lower intensities have been observed than at 300 K, indicating either the formation of higher and larger nanoparticles or an enhanced probability of intercalation/encapsulation during growth. An intensive intercalation can certainly be deduced from the STM images presented in Fig. 9 for low gold coverages (below 0.5 ML), where LEIS intensities exhibit a rather different behavior at the higher deposition temperature (Fig. 8). Fig. 9 presents a comparative measurement for Rh and Au deposited at 400 K on h-BN covered Rh(1 1 1) surface, followed by annealing at higher temperatures. The deposition of approximately 0.25 ML of Au at 400 K results in mainly 2D nanocrystallites with irregular outline, and with a single atomic layer thickness, and only a very little second layer deposit is observable (Fig. 9B1). Annealing at 500 K leads to some two-dimensional sintering of the particles without any significant change of their outline and flatness (B2). In this state, the h-BN layer does not show periodic nanomesh structure on gold surfaces. However, a clear modification of their top flatness can be observed after heat treatment at 700 K and especially at 1000 K (Fig. 9B3 and B4). Taking into account the present XPS / LEIS and our former results [24], we can exclude the formation of monoatomic thick 2D Au platelets on top of the h-BN layer at 400 K. It is much more probable that they are intercalated pure Au 2D nanoparticles, which start to form Au-Rh surface alloy as an effect of annealing at 700 K, and accordingly they show
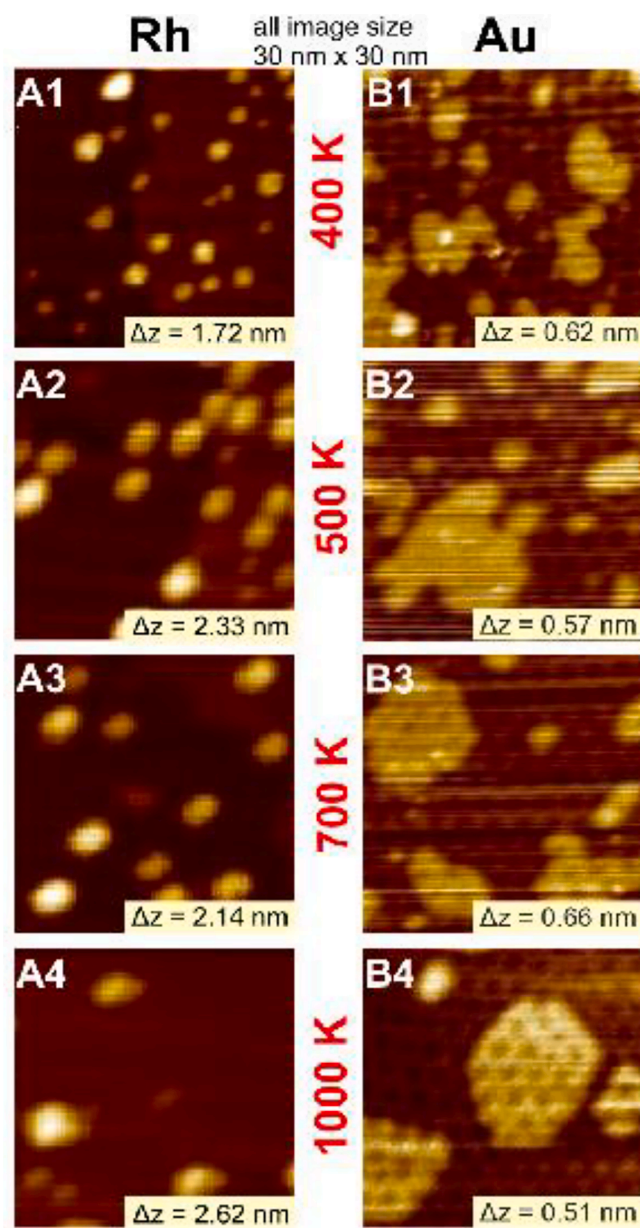
Fig. 9. STM images of 30 × 30 nm² recorded after the deposition of approximately 0.25 ML of (A1) Rh and (B1) Au on the h-BN covered Rh(1 1 1) surface at 400 K, followed by 5 min annealing at (B) 500 K, (C) 700 K, (D) 1000 K.

nanomesh structure at and above 700 K. Note that in this higher temperature range their outline became more and more regular and their perimeter strongly tailored by the hexagonal nanomesh lattice at 900 K (Fig. 9). In the case of Rh deposition, an analogue measurement exhibits a rather different behavior (Fig. 9A1–A4). At 400 K, Rh nanoparticles show different heights in the range of 0.2–0.8 nm, which indicates the formation of 2–4 layers high 3D particles of 2–4 nm diameter. The subsequent annealing treatments lead only to a slight and moderate sintering, and a gradual intercalation of Rh nanoparticles up to 1000 K. Although it cannot be inferred from STM images, encapsulation of Rh nanoparticles can also occur during the annealing process.

In order to facilitate the formation of extended 2D Rh nanoparticles underneath the h-BN net, a higher deposition temperature was required. In contrast to the results obtained after the deposition of Rh at lower temperatures (300–500 K), growth at 600 K (Fig. 10) obviously resulted in some 2D nanoparticles (Fig. 10A), apart from a greater number of 3D particles. One faint, but clearly visible extended 2D nanoparticle, with a
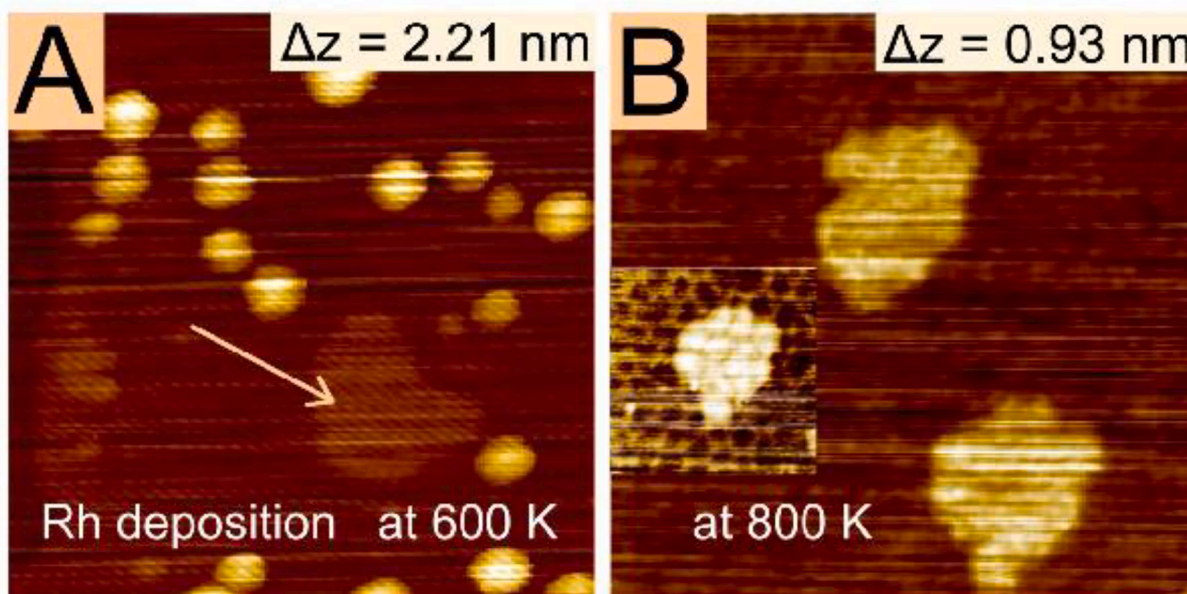
Fig. 10. STM images of 50 × 50 nm² recorded after the deposition of approximately 0.1–0.2 ML of Rh on to the h-BN covered Rh(1 1 1) surface at (A) 600 K and (B) 800 K sample temperatures (two independent experiments). The image of 30 nm × 30 nm inserted in (B) (left middle) reveals the presence of the periodic nanomesh also on the top of an intercalated 2D Rh nanoparticle.

height of approximately 0.2 nm, is indicated by an arrow on image (A). The height of 3D particles varies between 0.4 and 1.0 nm (2–5 atomic layers). By the application of even higher sample temperature (800 K) during the evaporation of Rh, one obtains only intercalated 2D Rh nanoparticles with a lateral extension of approximately 5–10 nm and with a thickness of a single atomic layer (Fig. 10B). The inserted image in (B) clearly shows that the top of the 2D nanoparticle exhibits the same nanomesh structure as that on Rh(1 1 1) support terraces.

3.4. Theoretical studies

DFT calculations were performed for several model systems outlined in Section 2. By comparing the h-BN layer on pure Rh(1 1 1) and on 1 ML Au on Rh(1 1 1) substrates, we found that the nanomesh structure is formed in the former case only, and in the latter case we obtain an atomically flat h-BN layer, as shown in Fig. 11A and B, respectively. For h-BN/Rh(1 1 1) (Fig. 11A) a geometric corrugation of the h-BN layer of 0.235 nm was found, and the smaller (~one third) apparent height observed in STM was also discussed [24,72]. The Rh-BN minimal vertical distance is 0.199 nm in the pore region. The DFT adsorption energy of the h-BN layer is −50.568 eV (-0.299 eV per BN unit), which is in very good agreement with that obtained by other DFT + vdW methods (revPBE-D3: −51 eV, PBE-rVV10: −50 eV) [73]. Moreover, the geometric corrugation (0.233 nm) of h-BN obtained by PBE-rVV10 reported in this reference is almost identical to our DFT result. On the other hand, the h-BN layer is atomically flat with a geometric corrugation of only 0.004 nm for the h-BN/Au$_{1ML}$/Rh(1 1 1) model system (Fig. 11B). The Au-BN minimal vertical distance is 0.337 nm. The adsorption energy of the h-BN layer in this case is −25.197 eV (−0.149 eV per BN unit), which is half of the value calculated on the stronger bound Rh(1 1 1) substrate, where the h-BN layer forms the nanomesh structure. With these results the fundamental difference of the h-BN layer formation on a pure Rh or Au covered Rh substrate is quantified.

The experimentally motivated assumption that Rh desorption has a larger activation energy than Au desorption is further confirmed by calculating the adsorption energy of individual Rh and Au adatoms on h-BN/Rh(1 1 1) with DFT. The relaxed adatom configurations are shown in Fig. 11C and D for the Rh and Au, respectively. The adsorption energy of the Au adatom is −3.21 eV in the energetically favored "on-top B in

pore" position, where the Au-B center-to-center distance is 0.214 nm, and the Au is negatively charged by 0.49 electrons [53]. On the other hand, the adsorption energy of Rh adatom is increased in absolute value to −4.69 eV in the energetically favored "on-top N in pore" position, where the Rh-N center-to-center distance is smaller, 0.203 nm (very close to the vertical Rh-BN distance of 0.199 nm observed in the strongest bound pore region of the h-BN layer in the nanomesh structure), and the Rh is negatively charged by 0.17 electrons. These results suggest that the surface diffusion probability of Rh atoms is much lower than that of Au adatoms. Moreover, the larger charge accumulated on Au adatoms may contribute to the lower nucleation probability of Au than of Rh, due to the dipole–dipole repulsion. The STM measurements presented in Section 3.3 support well these theoretical predictions.

We also found a substantial difference of atomic island formation considering model systems consisting of 19 atoms of Rh and Au (~0.13 ML coverage) after atomic geometry optimization minimizing the total energy in zero-temperature DFT calculations. The initially considered flat 2D atomic structures deposited on the pore region of the h-BN nanomesh on Rh(1 1 1) converged to a 3D two-atomic-layer thick Rh island (Fig. 11E), and, in stark contrast, to a bent 2D single-atomic-layer thick Au island (Fig. 11F) [53]. This finding is in line with the experimental observations presented in Section 3.3.

The driving force and some general mechanisms for the intercalation of both Rh and Au metals were further studied by DFT within relatively simple models. We focused on two aspects: total energy comparisons of adsorbed and intercalated metal structures on h-BN/Rh(1 1 1), and the role of simple defects in a free-standing h-BN layer (without a metal substrate) on metal atom adsorption. Total energy comparisons between the metal$_{1ML}$/h-BN/Rh(1 1 1) (Fig. 11G and H) and h-BN/metal$_{1ML}$/Rh(1 1 1) (Fig. 11A and B) model systems confirm that the monolayer metal always prefers to be located below the h-BN layer, in direct contact with the metal substrate. A similar comparison between metal$_{adatom}$/h-BN/Rh(1 1 1) (taken in the energetically favored adsorption positions: "on-top N in pore" for Rh and "on-top B in pore" for Au, see Fig. 11C and D) and h-BN/metal$_{atom}$/Rh(1 1 1) (atom below pore: Fig. 11I–J, atom below wire: Fig. 11K–L) models show that the intercalated individual metal atoms prefer to be located below the wire region of the h-BN nanomesh (Fig. 11K and L), and metal atom below the pore region is not preferred since it modifies the local structure of the h-BN layer in the pore making
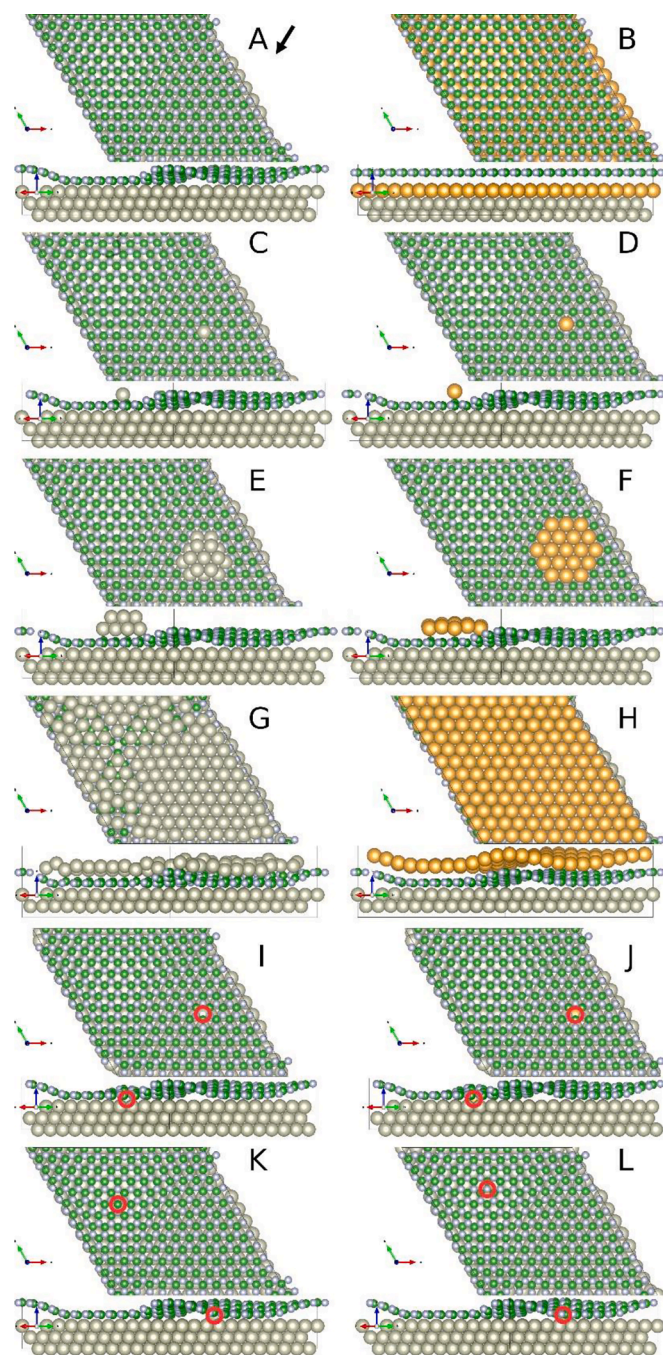
Fig. 11. Top and side views of the optimized atomic geometries of the studied model systems by DFT calculations: (A) h-BN/Rh(1 1 1), (B) h-BN/Au$_{1ML}$/Rh (1 1 1), (C) Rh$_{adatom}$/h-BN/Rh(1 1 1), (D) Au$_{adatom}$/h-BN/Rh(1 1 1), (E) Rh$_{19-atoms-island}$/h-BN/Rh(1 1 1), (F) Au$_{19-atoms-island}$/h-BN/Rh(1 1 1), (G) Rh$_{1ML}$/h-BN/Rh(1 1 1), (H) Au$_{1ML}$/h-BN/Rh(1 1 1), (I) h-BN/Rh$_{atom@pore}$/Rh(1 1 1), (J) h-BN/Au$_{atom@pore}$/Rh(1 1 1), (K) h-BN/Rh$_{atom@wire}$/Rh(1 1 1), (L) h-BN/Au$_{atom@wire}$/Rh(1 1 1). Atomic spheres and colors: Rh (large, grey), Au (large, yellow), B (small, green), N (small, grey). The black arrow beside "A" indicates the viewing direction of the side-view subfigures. The positions of the intercalated individual metal atoms below the h-BN layer are indicated by red circles in (I)–(L) for a better identification.

a weaker interaction to the Rh substrate, see Fig. 11I and J (side views). To quantify these findings, the total energy differences per metal atom are reported in Table 1, for the exact definition, see the caption. Rh clearly exhibits larger negative energy differences and smaller positive energy difference than Au, which suggests that Rh atomic intercalation

Table 1

Driving force for Rh and Au metal intercalation in h-BN/Rh(1 1 1): total energy differences per metal atom $\Delta E = (E_{h\text{-}BN/metal/Rh(1\,1\,1)} - E_{metal/h\text{-}BN/Rh(1\,1\,1)})/N_{metal}$ in eV units for 1 ML metal and a single atom considered in the pore and wire regions below the h-BN layer on Rh(1 1 1). Negative values mean that intercalation is preferred, while positive values indicate an unfavored intercalated structure.

ΔE (eV)	Rh	Au
1ML, Fig. 11A,B,G,H	−1.72	−0.59
single atom at pore, Fig. 11C,D,I,J	+1.17	+4.81
single atom at wire, Fig. 11C,D,K,L	−2.76	−1.42

is promoted compared to Au due to the presence of the Rh substrate. Overall, the driving force for the metal intercalation below the h-BN layer is the identified energy difference in the described model systems. Moreover, we found that the nanomesh structure of h-BN is conserved upon adsorption of 1 ML of Rh or Au on top. The metal adlayer perfectly follows the practically unchanged nanomesh structure for Au (Fig. 11H), while the Rh adlayer shows some reconstruction together with an increased diameter of the h-BN layer nanomesh (Fig. 11G). This calculation confirms the conclusion obtained from STM and LEIS measurements (Fig. 9B1 and B2 and Fig. 8B), that flat 2D gold nanoplates are localized at the h-BN/Rh(1 1 1) interface, and not on top of h-BN.

Total energies of a large number of atomic configurations of a Rh or Au metal atom on or within a free-standing h-BN layer without or with defects were calculated. The energetically best configurations on defected h-BN are shown in Fig. 12. As defects, single B vacancy (V$_B$, Fig. 12A–D), single N vacancy (V$_N$, Fig. 12E–H), and BN double vacancy (V$_{BN}$, Fig. 12I–P) were considered. Such defects are likely to form at elevated temperatures. Metal atom adsorption on h-BN was freely relaxed starting above B, N, hexagon and defect sites, resulting in energetically preferred "on-top N" configurations above the intact h-BN for both Rh and Au (note the qualitatively different "on-top B" Au adsorption on h-BN/Rh(1 1 1)), and best on-defect adsorption V$_B$, V$_N$, and V$_{BN}$ (above the middle of the BN double vacancy) for the corresponding defected h-BN layers (Fig. 12A,C,E,G,I,K). Metal atom adsorptions within the h-BN layer in hexagon and defect sites were relaxed in the plane. We find that unrelaxed hexagon sites are highly unfavored for in-plane metal adsorption in comparison to adatom adsorption on the h-BN. The reason is the size of the Rh and Au atoms, which can be accommodated within the hexagonal BN-ring only with a much-increased total energy. After performing in-plane relaxation considering metal atom at hexagon sites, the h-BN layer is much rearranged in the plane, and a defect is created by opening up a space equivalent of 7 BN-rings around the metal atom. The total energies of such configurations are still much larger than those of the found best adatom adsorption sites due to the rearrangement of the h-BN layer. From these results, we conclude that metal atom intercalation through hexagonal BN-rings is highly unfavorable energetically. The defect sites within the h-BN layer are much more preferred for metal adsorption than hexagon sites. The size of Rh and Au atoms is still large compared to the considered V$_B$, V$_N$, and V$_{BN}$ defects, which results in reduced metal-B,N distances (bonds when formed) and an increased total energy for such metal-in-BN-plane configurations.

The energy difference between the best adatom adsorption on the h-BN layer (Fig. 12A,C,E,G,I,K) and the best in-plane relaxed configuration (Fig. 12B,D,F,H,J,L,M–P) estimates an energy barrier for the atomic intercalation process when a metal atom moves from the given adsorption site to the h-BN layer. Such estimated atomic intercalation energy barriers are found to be much smaller for defected h-BN systems than for the hexagon sites, thus atomic intercalation through defects is better promoted. The results for the defected h-BN layers are summarized in Table 2, and the corresponding atomic configurations are shown in Fig. 12. Upon further analysis we find that the equilibrium metal-B,N nearest neighbor distances in the in-plane configurations of Fig. 12
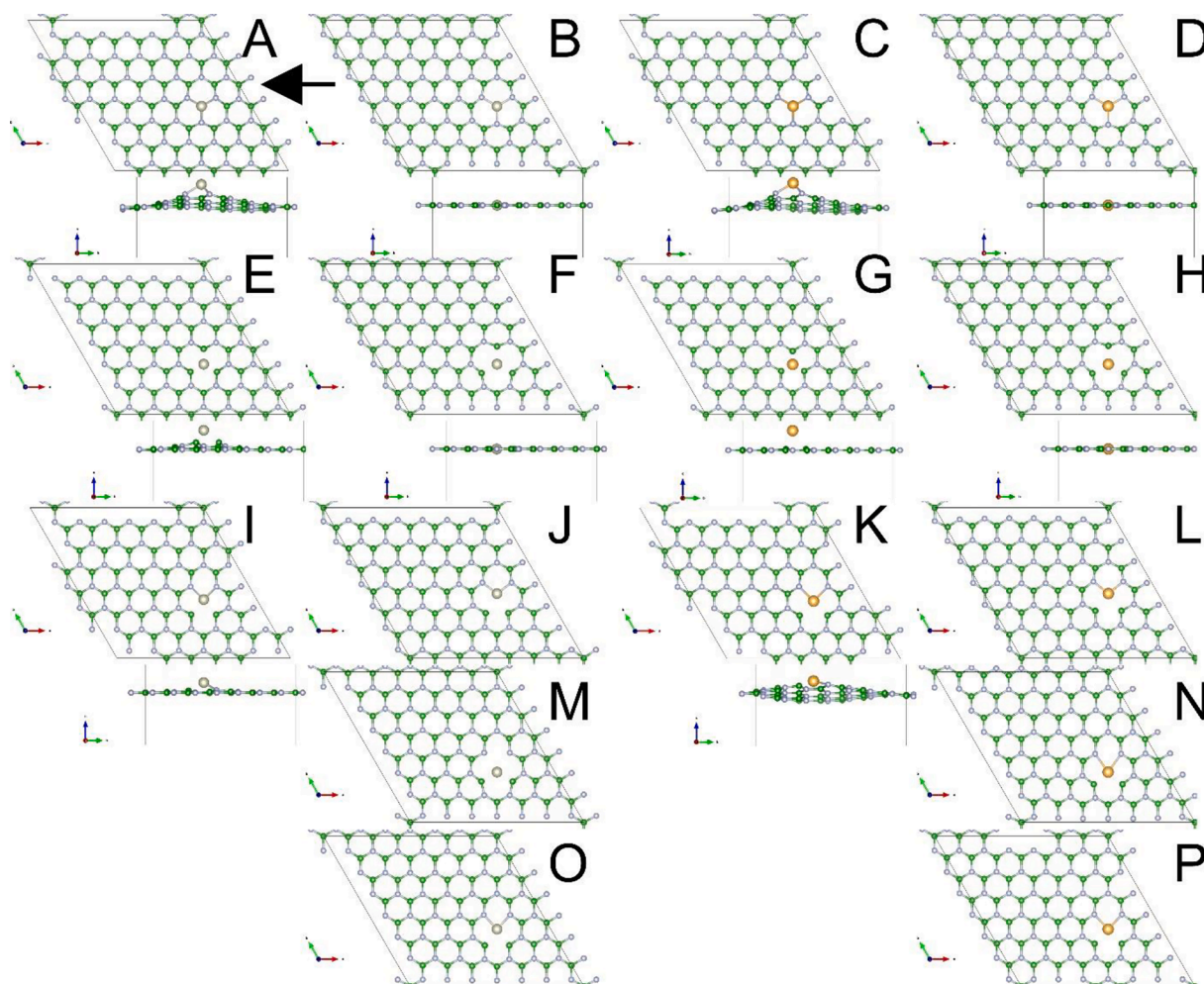
Fig. 12. Top and side views of the optimized atomic geometries of Rh and Au single metal atoms on or within a free-standing defected h-BN layer from DFT calculations: (A) h-BN(V_B): Rh on V_B, (B) h-BN(V_B): Rh in V_B, (C) h-BN(V_B): Au on V_B, (D) h-BN(V_B): Au in V_B, (E) h-BN(V_N): Rh on V_N, (F) h-BN(V_N): Rh in V_N, (G) h-BN (V_N): Au on V_N, (H) h-BN(V_N): Au in V_N, (I) h-BN(V_{BN}): Rh on V_{BN}, (J) h-BN(V_{BN}): Rh in V_B, (K) h-BN(V_{BN}): Au on V_{BN}, (L) h-BN(V_{BN}): Au in V_B, (M) h-BN(V_{BN}): Rh in V_N, (N) h-BN(V_{BN}): Au in V_N, (O) h-BN(V_{BN}): Rh in V_{BN}, (P) h-BN(V_{BN}): Au in V_{BN}. Atomic spheres and colors: Rh (large, grey), Au (large, yellow), B (small, green), N (small, grey). The black arrow beside "A" indicates the viewing direction of the side-view subfigures. Side views are not shown for (J),(L),(M)–(P) since the metal atom is located in the h-BN plane similarly to the side views of (B),(D),(F),(H). See the text and the caption of Table 2 for further details, and Table 2 for the related energetic comparisons.

Table 2

Estimated energy barriers for Rh and Au metal atom intercalation in free-standing defected h-BN: total energy differences $\Delta E = (E_{atom\ within\ h\text{-}BN\ layer} - E_{atom\ on\ h\text{-}BN\ layer})$ in eV units taking the best on-defect configuration as reference (second term in ΔE). The in-plane configurations (first term in ΔE) are denoted by h-BN(xx) @ yy, where defected h-BN is denoted by h-BN(xx = defect type), where the considered defect types are: V_B (B vacancy), V_N (N vacancy), and V_{BN} (BN double vacancy). The atomic positions within the h-BN layer (yy) are indicated by V_B, V_N, and V_{BN} (middle of the BN double vacancy). The corresponding atomic configurations in Fig. 12 are indicated in parentheses beside the estimated energy barrier values.

ΔE (eV)	Rh	Au
h-BN(V_B) @ V_B	4.5 (Fig. 12B,A)	4.8 (Fig. 12D,C)
h-BN(V_N) @ V_N	5.9 (Fig. 12F,E)	7.6 (Fig. 12H,G)
h-BN(V_{BN}) @ V_B	3.4 (Fig. 12J,I)	3.3 (Fig. 12L,K)
h-BN(V_{BN}) @ V_N	4.3 (Fig. 12M,I)	3.3 (Fig. 12N,K)
h-BN(V_{BN}) @ V_{BN}	2.1 (Fig. 12O,I)	0.9 (Fig. 12P,K)

deviate from those of the energy minimum corresponding to the metal-on-BN configurations: the larger the absolute distance deviation the larger the energy difference (not shown). We find that V_N defect sites show at least the same or higher energy barrier than V_B sites. The middle

of a V_{BN} defect was overall the best adsorption site within the h-BN layer (Fig. 12O,P), resulting in only 0.9–2.1 eV energy barrier as described above. The reason is that the Rh and Au atoms fit the best to the V_{BN} defect due to its size among the considered three simple defects. The identified trend of our results also suggests that h-BN defects with larger spatial extension and h-BN edges could play an even more important role in metal intercalation processes. According to Table 2, we also found that Au has systematically larger energy barriers than Rh for the V_B- and V_N- defected h-BN layers, but not for the V_{BN}-defected h-BN layer, where the Rh shows larger energy barrier than Au, irrespectively of the defect site type V_B, V_N, or V_{BN}. The above findings demonstrate that the atomic intercalation energy barrier depends on both the defect type and the atomic species. Moreover, since the metal support is missing in our model calculations here, we expect that the presence of the Rh support promotes Rh compared to Au atomic intercalation, as discussed before. Going beyond these DFT findings, for further research we propose the employment of reaction kinetics calculations for such simple defects and larger defected h-BN/substrate systems and diffusion of metal atoms at h-BN edges for a more detailed microscopic understanding of the metal intercalation mechanism, which could not be performed up to now due to the computationally demanding systems.

4. Conclusions

In this work rhodium and gold nanoparticles were grown on a Rh (111) substrate covered by hexagonal boron nitride nanomesh, and their structural and thermal properties were compared based on LEIS, STM, and XPS results, which have been corroborated/complemented by DFT calculations. Upon physical vapor deposition at 300 K substrate temperature, both metals follow characteristically Volmer-Weber (3D) growth, since metal–metal interaction is much stronger than the interaction with h-BN. While previous studies revealed nearly 2D growth of gold at small coverages (~0.1 ML), the present DFT calculations in accordance with LEIS results indicate 3D growth even for small Rh clusters. This difference likely stems from the stronger Rh-Rh interaction, when compared to Au-Au interaction. Annealing treatments activate various phenomena, and significant differences have been revealed in the behavior of rhodium and gold. Based on LEIS results, four characteristic temperature ranges (T-Range) can be identified. Although these intervals were a bit different for the two metals, the characteristic processes are listed in Table 3, where the dominant ones are shown boldfaced.

In T-Range I, only smaller or moderate changes have been found by all three experimental methods, attributed mostly to sintering/ agglomeration. In T-Range II, a steep attenuation of the admetal LEIS intensity took place. Taking into account STM and XPS data as well, it was concluded that for rhodium an encapsulation phenomenon is the dominant process in T-Range II, implying the diffusion of boron nitride fragments onto Rh nanoparticles from their bottom region. The first step here is the rupture of B–N bonds by the reactive Rh nanoparticles. Defects created in h-BN may serve as intercalation channels. In spite of the quicker diffusion of gold on h-BN, the steep intensity loss in LEIS has been observed at higher temperatures for the gold deposit (see Table 3), very probably because it cannot catalyze the B–N bond scission. Instead, the intensity loss stems from the intercalation of gold below h-BN, as confirmed by XPS. However, we cannot exclude that sufficiently small gold nanoparticles, which are more reactive, can initiate the encapsulation process.

In T-Range III, encapsulated Rh nanoparticles flatten out, and two-dimensional sintering below h-BN takes place similar to 3D Ostwald ripening. In the case of gold, intercalation is one dominant process in this T-Range. Intercalated atoms diffuse to Rh steps, moreover the Au-Rh exchange is also activated, and consequently no 2D islands form. According to quantitative XPS analysis, the desorption of gold is the other dominant process in this temperature range. It is more difficult to estimate the extent of Rh desorption, since the substrate is also Rh.

In T-Range IV, around 1150 K–1200 K, the decomposition of h-BN by the substrate sets in. The accumulation of gold at the h-BN–Rh(111) interface efficiently stabilizes the boron nitride monolayer due to the lower reactivity of gold, especially as a smooth film. The h-BN overlayer in turn hinders the desorption of Au from the surface at 1200 K. Therefore, the intercalation of Au is a one way process.

The effect of substrate temperature during metal deposition was also studied. The intercalation of gold atoms turned out to be very efficient during deposition at 400 K, presumably because isolated gold atoms are able to diffuse to defect sites of h-BN, and can penetrate through them at this temperature. Concerning this point, a fantastic agreement was found between DFT and our experimental methods (STM and LEIS). Although our experimental methods clearly revealed that the flat 2D gold plates, formed during deposition at 400 K, cannot be located on top of h-BN, but at the h-BN/Rh(111) interface, DFT calculation further confirmed that 2D Au plates on top of h-BN would follow the nanomesh morphology. A similar effect of the deposition temperature has been observed for Rh at much higher values (600 K–800 K), very probably because of the higher activation energy of Rh diffusion. This is approximately the temperature range (T-Range II), where the rupture of h-BN by Rh has been demonstrated (Table 3). It seems reasonable to assume that Rh atoms diffusing during deposition at 600 K–800 K can

Table 3
Thermally activated processes for Rh an Au, deposited at room temperature, classified according to characteristic temperature ranges. Dominant processes are listed boldfaced, while marginal or hypothetical processes are put in parenthesis.

	Rh	Au
T-Range I	300 K–550 K **sintering**	300 K–700 K **sintering**
T-Range II	600 K–750 K **encapsulation**, sintering, (intercalation)	700 K–850 K **intercalation**, (encapsulation)
T-Range III	800 K–1100 K **flattening and intercalation, 2D sintering below h-BN**, (desorption)	900 K–1100 K **intercalation,** 2D step flow growth below h-BN, **desorption**
T-Range IV	1150 K–1200 K **2D sintering, h-BN opening**	1150 K–1200 K **suppressed h-BN opening**

create defects in h-BN, which facilitate their intercalation.

DFT results confirmed that Rh desorption has a larger activation energy than Au desorption by calculating the adsorption energies of individual Rh and Au adatoms on the nanomesh. While both Rh and Au atoms prefer adsorption in the pore region, the Rh-N and Au-B bondings are preferred, which act as nucleation sites for the formation of larger metallic clusters. The negatively charged adatoms (0.49 and 0.17 electrons for Au and Rh, respectively) suggest single atom catalytic potential for these structures. Energetic preference for Rh and Au metal atom intercalation below the h-BN layer was found for different model systems. Finally, energy barriers for the Rh and Au atomic intercalation were estimated by considering a free-standing h-BN layer with various simple defects. We found that nitrogen vacancies show generally higher energy barrier for atomic intercalation than boron vacancies, and the energy barrier relation between Rh and Au critically depends on the h-BN defect type. Intercalation through the middle of a BN-divacancy provided the smallest energy barriers. Our identified trend points to the potential importance of h-BN defects with larger spatial extension and h-BN edges for metal intercalation processes. It is also anticipated that the presence of the Rh support promotes Rh compared to Au atomic intercalation through the h-BN layer.

CRediT authorship contribution statement

Gábor Vári: Investigation, Data curation, Visualization, Writing – review & editing. **Csaba Vass:** Investigation, Writing – review & editing. **Gyula Halasi:** Investigation, Writing – review & editing. **László Szabó:** Investigation. **Krisztián Palotás:** Conceptualization, Methodology, Software, Validation, Formal analysis, Investigation, Writing – review & editing, Visualization, Funding acquisition. **Péter Dombi:** Writing – review & editing, Supervision. **András Berkó:** Conceptualization, Formal analysis, Investigation, Data curation, Writing – original draft, Writing – review & editing, Visualization, Supervision. **László Óvári:** Conceptualization, Formal analysis, Data curation, Writing – original draft, Writing – review & editing, Visualization, Supervision, Project administration. **Zoltán Kónya:** Conceptualization, Writing – review & editing, Supervision, Funding acquisition.

Declaration of Competing Interest

The authors declare that they have no known competing financial interests or personal relationships that could have appeared to influence the work reported in this paper.

Data availability

The data that has been used is confidential.

Appendix A. Supplementary material

Supplementary data to this article can be found online at https://doi.org/10.1016/j.apsusc.2023.157041.

References

[1] A. Pakdel, Y. Bando, D. Golberg, Nano boron nitride flatland, Chem. Soc. Rev. 43 (2014) 934–959, https://doi.org/10.1039/c3cs60260e.

[2] W. Auwärter, Hexagonal boron nitride monolayers on metal supports: Versatile templates for atoms, molecules and nanostructures, Surf. Sci. Rep. 74 (2019) 1–95, https://doi.org/10.1016/j.surfrep.2018.10.001.

[3] M. Xu, T. Liang, M. Shi, H. Chen, Graphene-like two-dimensional materials, Chem. Rev. 113 (2013) 3766–3798, https://doi.org/10.1021/cr300263a.

[4] H. Agarwal, B. Terrés, L. Orsini, A. Montanaro, V. Sorianello, M. Pantouvaki, K. Watanabe, T. Taniguchi, D. Van Thourhout, M. Romagnoli, F.H.L. Koppens, 2D–3D integration of hexagonal boron nitride and a high-κ dielectric for ultrafast graphene-based electro-absorption modulators, Nat. Commun. 12 (2021) 1070, https://doi.org/10.1038/s41467-021-20926-w.

[5] M.-W. Chen, HoKwon Kim, C. Bernard, M. Pizzochero, J. Zaldívar, J.I. Pascual, M. M. Ugeda, O.V. Yazyev, T. Greber, J. Osterwalder, O. Renault, A. Kis, Electronic properties of transferable atomically thin MoSe 2 /h-BN heterostructures grown on Rh(111), ACS Nano 12 (11) (2018) 11161–11168, https://doi.org/10.1021/acsnano.8b05628.

[6] M. Yankowitz, J. Xue, B.J. LeRoy, Graphene on hexagonal boron nitride, J. Phys. Condens. Matter. 26 (30) (2014) 303201, https://doi.org/10.1088/0953-8984/26/30/303201.

[7] M.T. Paffett, R.J. Simonson, P. Papin, R.T. Paine, Borazine adsorption and decomposition at Pt(111) and Ru(001) surfaces, Surf. Sci. 232 (1990) 286–296, https://doi.org/10.1016/0039-6028(90)90121-N.

[8] A. Nagashima, N. Tejima, Y. Gamou, T. Kawai, C. Oshima, Electronic dispersion relations of monolayer hexagonal boron nitride formed on the Ni(111) surface, Phys. Rev. B. 51 (1995) 4606–4613, https://doi.org/10.1103/PhysRevB.51.4606.

[9] M. Corso, W. Auwärter, M. Muntwiler, A. Tamai, T. Greber, J. Osterwalder, Boron Nitride Nanomesh, Science (80-.) 303 (2004) 217–220, https://doi:10.1126/science.1091979.

[10] A.B. Preobrajenski, A.S. Vinogradov, N. Mårtensson, Monolayer of h-BN chemisorbed on Cu(1 1 1) and Ni(1 1 1): The role of the transition metal 3d states, Surf. Sci. 582 (2005) 21–30, https://doi.org/10.1016/j.susc.2005.02.047.

[11] S. Joshi, D. Ecija, R. Koitz, M. Iannuzzi, A.P. Seitsonen, J. Hutter, H. Sachdev, S. Vijayaraghavan, F. Bischoff, K. Seufert, J.V. Barth, W. Auwärter, Boron nitride on Cu(111): An electronically corrugated monolayer, Nano Lett. 12 (2012) 5821–5828, https://doi.org/10.1021/nl303170m.

[12] M. Morscher, M. Corso, T. Greber, J. Osterwalder, Formation of single layer h-BN on Pd(111), Surf. Sci. 600 (2006) 3280–3284, https://doi.org/10.1016/j.susc.2006.06.016.

[13] A. Goriachko, Y. He, M. Knapp, H. Over, M. Corso, T. Brugger, S. Berner, J. Osterwalder, T. Greber, Self-Assembly of a Hexagonal Boron Nitride Nanomesh on Ru(0001), Langmuir 23 (2007) 2928–2931, https://doi.org/10.1021/la062990t.

[14] A.B. Preobrajenski, M.A. Nesterov, M.L. Ng, A.S. Vinogradov, N. Mårtensson, Monolayer h-BN on lattice-mismatched metal surfaces: On the formation of the nanomesh, Chem. Phys. Lett. 446 (2007) 119–123, https://doi.org/10.1016/j.cplett.2007.08.028.

[15] E. Ćavar, R. Westerström, A. Mikkelsen, E. Lundgren, A.S. Vinogradov, M.L. Ng, A. B. Preobrajenski, A.A. Zakharov, N. Mårtensson, A single h-BN layer on Pt(111), Surf. Sci. 602 (2008) 1722–1726, https://doi.org/10.1016/j.susc.2008.03.008.

[16] F. Müller, S. Hüfner, H. Sachdev, R. Laskowski, P. Blaha, K. Schwarz, Epitaxial growth of hexagonal boron nitride on Ag(111), Phys. Rev. B. 82 (2010), 113406, https://doi.org/10.1103/PhysRevB.82.113406.

[17] I. Brihuega, C.H. Michaelis, J. Zhang, S. Bose, V. Sessi, J. Honolka, M. Alexander Schneider, A. Enders, K. Kern, Electronic decoupling and templating of Co nanocluster arrays on the boron nitride nanomesh, Surf. Sci. 602 (2008) L95–L99, https://doi.org/10.1016/j.susc.2008.04.040.

[18] G. Dong, E.B. Fourré, F.C. Tabak, J.W.M. Frenken, How boron nitride forms a regular nanomesh on Rh(111), Phys. Rev. Lett. 104 (2010), 096102, https://doi.org/10.1103/PhysRevLett.104.096102.

[19] M. Corso, T. Greber, J. Osterwalder, H-BN on Pd(1 1 0): A tunable system for self-assembled nanostructures? Surf. Sci. 577 (2005) L78–L84, https://doi.org/10.1016/j.susc.2005.01.015.

[20] M. Thaler, D. Steiner, A. Menzel, F. Mittendorfer, E. Bertel, Single-domain h-BN on Pt (110): Electronic structure, correlation, and bonding, Physcal Rev. Res. 2 (2020), 043156, https://doi.org/10.1103/PhysRevResearch.2.043156.

[21] N.A. Vinogradov, A.A. Zakharov, M.L. Ng, A. Mikkelsen, E. Lundgren, N. Mårtensson, A.B. Preobrajenski, One-dimensional corrugation of the h-BN monolayer on Fe(110), Langmuir 28 (2012) 1775–1781, https://doi.org/10.1021/la2035642.

[22] K. Ali, L. Fernández, M.A. Kherelden, A.A. Makarova, I. Píš, F. Bondino, J. Lawrence, D.G. de Oteyza, D.Y. Usachov, D.V. Vyalikh, F.J. García de Abajo, Z. M.A. El-Fattah, J.E. Ortega, F. Schiller, Atomically-precise texturing of hexagonal boron nitride nanostripes, Adv. Sci. 8 (2021) 2101455, https://doi.org/10.1002/advs.202101455.

[23] R. Stania, W. Heckel, I. Kalichava, C. Bernard, T.C. Kerscher, H.Y. Cun, P. R. Willmott, B. Schönfeld, J. Osterwalder, S. Müller, T. Greber, Self-assembly of nanoscale lateral segregation profiles, Phys. Rev. B. 93 (2016), 161402, https://doi.org/10.1103/PhysRevB.93.161402.

[24] R. Gubó, G. Vári, J. Kiss, A.P. Farkas, K. Palotás, L. Óvári, A. Berkó, Z. Kónya, Tailoring the hexagonal boron nitride nanomesh on Rh(111) with gold, Phys. Chem. Chem. Phys. 20 (2018) 15473–15485, https://doi.org/10.1039/C8CP00790J.

[25] R. Laskowski, P. Blaha, K. Schwarz, Bonding of hexagonal BN to transition metal surfaces: An ab initio density-functional theory study, Phys. Rev. B. 78 (2008), 045409, https://doi.org/10.1103/PhysRevB.78.045409.

[26] J. Gómez Díaz, Y. Ding, R. Koitz, A.P. Seitsonen, M. Iannuzzi, J. Hutter, Hexagonal boron nitride on transition metal surfaces, Theor. Chem. Acc. 132 (2013) 1350, https://doi.org/10.1007/s00214-013-1350-z.

[27] M. Schwarz, A. Riss, M. Garnica, J. Ducke, P.S. Deimel, D.A. Duncan, P.K. Thakur, T.-L. Lee, A.P. Seitsonen, J.V. Barth, F. Allegretti, W. Auwärter, Corrugation in the weakly interacting hexagonal-BN/Cu(111) system: Structure determination by combining noncontact atomic force microscopy and X-ray standing waves, ACS Nano. 11 (2017) 9151–9161, https://doi.org/10.1021/acsnano.7b04022.

[28] L. Camilli, E. Sutter, P. Sutter, Growth of two-dimensional materials on non-catalytic substrates: h-BN/Au(111), 2D Mater. 1 (2014), https://doi.org/10.1088/2053-1583/1/2/025003.

[29] D. Usachov, V.K. Adamchuk, D. Haberer, A. Grüneis, H. Sachdev, A. B. Preobrajenski, C. Laubschat, D.V. Vyalikh, Quasifreestanding single-layer hexagonal boron nitride as a substrate for graphene synthesis, Phys. Rev. B. 82 (2010), 075415, https://doi.org/10.1103/PhysRevB.82.075415.

[30] M. Cattelan, B. Markman, G. Lucchini, P.K. Das, I. Vobornik, J.A. Robinson, S. Agnoli, G. Granozzi, New strategy for the growth of complex heterostructures based on different 2D materials, Chem. Mater. 27 (2015) 4105–4113, https://doi.org/10.1021/acs.chemmater.5b01170.

[31] R. Laskowski, P. Blaha, Unraveling the structure of the h-BN/Rh(111) nanomesh with ab initio calculations, J. Phys. Condens. Matter. 20 (6) (2008) 064207, https://doi.org/10.1088/0953-8984/20/6/064207.

[32] S. Berner, M. Corso, R. Widmer, O. Groening, R. Laskowski, P. Blaha, K. Schwarz, A. Goriachko, H. Over, S. Gsell, M. Schreck, H. Sachdev, T. Greber, J. Osterwalder, Boron nitride nanomesh: Functionality from a corrugated monolayer, Angew. Chemie Int. Ed. 46 (2007) 5115–5119, https://doi.org/10.1002/anie.200700234.

[33] F. Orlando, P. Lacovig, L. Omiciuolo, N.G. Apostol, R. Larciprete, A. Baraldi, S. Lizzit, Epitaxial growth of a single-domain hexagonal boron nitride monolayer, ACS Nano. 8 (2014) 12063–12070, https://doi.org/10.1021/nn5058968.

[34] F.H. Farwick zum Hagen, D.M. Zimmermann, C.C. Silva, C. Schlueter, N. Atodiresei, W. Jolie, A.J. Martínez-Galera, D. Dombrowski, U.A. Schröder, M. Will, P. Lazić, V. Caciuc, S. Blügel, T.-L. Lee, T. Michely, C. Busse, Structure and growth of hexagonal boron nitride on Ir(111), ACS Nano 10 (12) (2016) 11012–11026, https://doi.org/10.1021/acsnano.6b05819.

[35] M. Petrović, U. Hagemann, M. Horn-von, F.-j. Hoegen, Meyer zu Heringdorf, Microanalysis of single-layer hexagonal boron nitride islands on Ir(111), Appl. Surf. Sci. 420 (2017) 504–510, https://doi.org/10.1016/j.apsusc.2017.05.155.

[36] Y. Qi, N. Han, Y. Li, Z. Zhang, X. Zhou, B. Deng, Q. Li, M. Liu, J. Zhao, Z. Liu, Y. Zhang, Strong Adlayer-substrate interactions "Break" the patching growth of h-BN onto graphene on Re(0001), ACS Nano. 11 (2017) 1807–1815, https://doi.org/10.1021/acsnano.6b07773.

[37] W. Auwärter, M. Muntwiler, T. Greber, J. Osterwalder, Co on h-BN/Ni (1 1 1): from island to island-chain formation and Co intercalation, Surf. Sci. 511 (2002) 379–386, https://doi.org/10.1016/S0039-6028(02)01545-5.

[38] M.L. Ng, A.B. Preobrajenski, A.S. Vinogradov, N. Mårtensson, Formation and temperature evolution of Au nanoparticles supported on the h-BN nanomesh, Surf. Sci. 602 (2008) 1250–1255, https://doi.org/10.1016/j.susc.2008.01.028.

[39] A. Goriachko, Y.B. He, H. Over, Complex growth of NanoAu on BN nanomeshes supported by Ru(0001), J. Phys. Chem. C. 112 (2008) 8147–8152, https://doi.org/10.1021/jp7119608.

[40] H.P. Koch, R. Laskowski, P. Blaha, K. Schwarz, Adsorption of gold atoms on the h-BN/Rh(111) nanomesh, Phys. Rev. B. 84 (2011) 245410, https://doi.org/10.1103/PhysRevB.84.245410.

[41] H.P. Koch, R. Laskowski, P. Blaha, K. Schwarz, Adsorption of small gold clusters on the h-BN/Rh(111) nanomesh, Phys. Rev. B. 86 (2012) 155404, https://doi.org/10.1103/PhysRevB.86.155404.

[42] Y. Zhang, Y. Zhang, D. Ma, Q. Ji, W. Fang, J. Shi, T. Gao, M. Liu, Y. Gao, Y. Chen, L. Xu, Z. Liu, Mn atomic layers under inert covers of graphene and hexagonal boron nitride prepared on Rh(111), Nano Res. 6 (2013) 887–896, https://doi.org/10.1007/s12274-013-0365-z.

[43] M.C. Patterson, B.F. Habenicht, R.L. Kurtz, L. Liu, Y. Xu, P.T. Sprunger, Formation and stability of dense arrays of Au nanoclusters on hexagonal boron nitride/Rh

(111), Phys. Rev. B - Condens. Matter Mater. Phys. 89 (2014), 205423, https://doi.org/10.1103/PhysRevB.89.205423.

[44] W.C. McKee, M.C. Patterson, D. Huang, J.R. Frick, R.L. Kurtz, P.T. Sprunger, L. Liu, Y. Xu, CO Adsorption on Au nanoparticles grown on hexagonal boron nitride/Rh (111), J. Phys. Chem. C. 120 (2016) 10909–10918, https://doi.org/10.1021/acs.jpcc.6b01645.

[45] W.C. McKee, M.C. Patterson, J.R. Frick, P.T. Sprunger, Y. Xu, Adsorption of transition metal adatoms on h-BN/Rh(111): Implications for nanocluster self-assembly, Catal. Today. 280 (2017) 220–231, https://doi.org/10.1016/j.cattod.2016.09.030.

[46] F. Düll, M. Meusel, F. Späth, S. Schötz, U. Bauer, P. Bachmann, J. Steinhauer, H.-P. Steinrück, A. Bayer, C. Papp, Growth and stability of Pt nanoclusters from 1 to 50 atoms on h-BN/Rh(111), Phys. Chem. Chem. Phys. 21 (2019) 21287–21295, https://doi.org/10.1039/C9CP04095A.

[47] M. Will, T. Hartl, V. Boix de la Cruz, P. Lacovig, S. Lizzit, J. Knudsen, T. Michely, P. Bampoulis, Growth, stability, and electronic decoupling of Pt clusters on h-BN/Ir (111), J. Phys. Chem. C. 125 (2021) 3880–3889, https://doi.org/10.1021/acs.jpcc.0c10136.

[48] M. Will, N. Atodiresei, V. Caciuc, P. Valerius, C. Herbig, T. Michely, A monolayer of hexagonal boron nitride on Ir(111) as a template for cluster superlattices, ACS Nano. 12 (2018) 6871–6880, https://doi.org/10.1021/acsnano.8b02127.

[49] Á. Szitás, R. Gubó, T. Pásztor, A.P. Farkas, T. Ajtai, L. Óvári, K. Palotás, A. Berkó, Z. Kónya, Adsorption of azobenzene on hexagonal boron nitride nanomesh supported by Rh(111), J. Phys. Chem. C. 124 (2020) 14182–14194, https://doi.org/10.1021/acs.jpcc.0c01725.

[50] F. Wu, D. Huang, Y. Yue, L. Liu, Template growth of Au, Ni and Ni–Au nanoclusters on hexagonal boron nitride/Rh(111): A combined STM, TPD and AES study, RSC Adv. 7 (2017) 44169–44177, https://doi.org/10.1039/C7RA08880A.

[51] Y. Fukamori, M. König, B. Yoon, B. Wang, F. Esch, U. Heiz, U. Landman, Fundamental insight into the substrate-dependent ripening of monodisperse clusters, ChemCatChem. 5 (2013) 3330–3341, https://doi.org/10.1002/cctc.201300250.

[52] A.P. Farkas, Á. Szitás, G. Vári, R. Gubó, L. Óvári, A. Berkó, J. Kiss, Z. Kónya, Effect of gold on the adsorption properties of acetaldehyde on clean and h-BN covered Rh (111) surface, Top. Catal. 61 (2018) 1247–1256, https://doi.org/10.1007/s11244-018-0979-1.

[53] A.P. Farkas, Á. Szitás, D. Jurdi, K. Palotás, J. Kiss, Z. Kónya, Selective transformation of ethanol to acetaldehyde catalyzed by Au/h-BN interface prepared on Rh(111) surface, Appl. Catal. A Gen. 592 (2020), 117440, https://doi.org/10.1016/j.apcata.2020.117440.

[54] F. Düll, J. Steinhauer, F. Späth, U. Bauer, P. Bachmann, H.-P. Steinrück, S. Wickert, R. Denecke, C. Papp, Ethylene: Its adsorption, reaction, and coking on Pt/ h -BN/ Rh(111) nanocluster arrays, J. Chem. Phys. 152 (22) (2020) 224710, https://doi.org/10.1063/5.0011616.

[55] L. Liu, Z. Zhou, Q. Guo, Z. Yan, Y. Yao, D.W. Goodman, The 2-D growth of gold on single-layer graphene/Ru(0001): Enhancement of CO adsorption, Surf. Sci. 605 (2011) L47–L50, https://doi.org/10.1016/j.susc.2011.04.040.

[56] L. Óvári, A. Berkó, G. Vári, R. Gubó, A.P. Farkas, Z. Kónya, The growth and thermal properties of Au deposited on Rh(111): Formation of an ordered surface alloy, Phys. Chem. Chem. Phys. 18 (2016) 25230–25240, https://doi.org/10.1039/C6CP02128J.

[57] H. Okamoto, T.B. Massalski, The Au-Rh (Gold-Rhodium) System, Bull. Alloy Phase Diagrams. 5 (4) (1984) 384–387.

[58] J. Cazaux, T. Bardoux, D. Mouze, J.M. Patat, G. Salace, X. Thomas, J. Tóth, Preliminary results on multiple angular detection Auger spectroscopy, Surf. Interface Anal. 19 (1992) 197–199, https://doi.org/10.1002/sia.740190138.

[59] G. Kresse, J. Furthmüller, Efficient iterative schemes for ab initio total-energy calculations using a plane-wave basis set, Phys. Rev. B. 54 (1996) 11169–11186, https://doi.org/10.1103/PhysRevB.54.11169.

[60] G. Kresse, J. Furthmüller, Efficiency of ab-initio total energy calculations for metals and semiconductors using a plane-wave basis set, Comput. Mater. Sci. 6 (1996) 15–50, https://doi.org/10.1016/0927-0256(96)00008-0.

[61] G. Kresse, D. Joubert, From ultrasoft pseudopotentials to the projector augmented-wave method, Phys. Rev. B. 59 (1999) 1758–1775, https://doi.org/10.1103/PhysRevB.59.1758.

[62] J. Klimeš, D.R. Bowler, A. Michaelides, Chemical accuracy for the van der Waals density functional, J. Phys. Condens. Matter. 22 (2) (2010) 022201, https://doi.org/10.1088/0953-8984/22/2/022201.

[63] J. Klimeš, D.R. Bowler, A. Michaelides, Van der Waals density functionals applied to solids, Phys. Rev. B. 83 (2011), 195131, https://doi.org/10.1103/PhysRevB.83.195131.

[64] H.P. Singh, Determination of thermal expansion of germanium, rhodium and iridium by X-rays, Acta Crystallogr. Sect. A. 24 (1968) 469–471, https://doi.org/10.1107/S056773946800094X.

[65] O. Bunk, M. Corso, D. Martoccia, R. Herger, P.R. Willmott, B.D. Patterson, J. Osterwalder, J.F. van der Veen, T. Greber, Surface X-ray diffraction study of boron-nitride nanomesh in air, Surf. Sci. 601 (2007) L7–L10, https://doi.org/10.1016/j.susc.2006.11.018.

[66] H.H. Brongersma, M. Draxler, M. de Ridder, P. Bauer, Surface composition analysis by low-energy ion scattering, Surf. Sci. Rep. 62 (2007) 63–109, https://doi.org/10.1016/j.surfrep.2006.12.002.

[67] J.H. Scofield, Hartree-Slater subshell photoionization cross-sections at 1254 and 1487 eV, J. Electron Spectros. Relat. Phenomena. 8 (1976) 129–137, https://doi.org/10.1016/0368-2048(76)80015-1.

[68] S. Tanuma, C.J. Powell, D.R. Penn, Calculations of electron inelastic mean free paths, Surf. Interface Anal. 21 (1994) 165–176, https://doi.org/10.1002/sia.1997.

[69] Q. Fu, T. Wagner, Interaction of nanostructured metal overlayers with oxide surfaces, Surf. Sci. Rep. 62 (2007) 431–498, https://doi.org/10.1016/j.surfrep.2007.07.001.

[70] L. Óvári, A. Berkó, R. Gubó, Á. Rácz, Z. Kónya, Effect of a gold cover layer on the encapsulation of rhodium by titanium oxides on titanium dioxide (110), J. Phys. Chem. C. 118 (2014) 12340–12352, https://doi.org/10.1021/jp502748a.

[71] M. Mavrikakis, P. Stoltze, J.K. Nørskov, Making gold less noble, Catal. Letters. 64 (2000) 101–106, https://doi.org/10.1023/A:1019028229377.

[72] W.C. McKee, V. Meunier, Y. Xu, Reconciling the electronic and geometric corrugations of the hexagonal boron nitride and graphene nanomeshes, Surf. Sci. 642 (2015) L16–L19, https://doi.org/10.1016/j.susc.2015.06.014.

[73] M. Iannuzzi, F. Tran, R. Widmer, T. Dienel, K. Radican, Y. Ding, J. Hutter, O. Gröning, Site-selective adsorption of phthalocyanine on h-BN/Rh(111) nanomesh, Phys. Chem. Chem. Phys. 16 (2014) 12374–12384, https://doi.org/10.1039/c4cp01466a.